Structural architecture and maturity of Val d'Agri faults, Italy: Inferences from natural and induced seismicity

G. Schirripa Spagnolo [a,*], F. Agosta [b], L. Aldega [a], G. Prosser [b], L. Smeraglia [c], S. Tavani [c,d], N. Looser [e], M. Guillong [e], S.M. Bernasconi [e], A. Billi [c], E. Carminati [a]

[a] Dipartimento di Scienze Della Terra, Sapienza Università di Roma, Piazzale Aldo Moro 5, 00185, Roma, Italy
[b] Dipartimento di Scienze, Università Della Basilicata, Via Dell'Ateneo Lucano, 10 - 85100, Potenza, Italy
[c] Consiglio Nazionale Delle Ricerche, IGAG, c.o. Dipartimento di Scienze Della Terra, Sapienza Università di Roma, P.le Aldo Moro 5, 00185, Roma, Italy
[d] DISTAR, Università Degli Studi di Napoli Federico II, Via Cupa Nuova Cintia, 21, 80126, Napoli, Italy
[e] Department of Earth Sciences, ETH Zurich, Sonneggstrasse 5, 8092, Zürich, Switzerland

A B S T R A C T

The Val d'Agri Basin is a Quaternary sedimentary basin topping multiple tectonic units of the southern Apennines fold-and-thrust belt and a giant oilfield within deeper Apulian Platform carbonates. This basin is bounded by the seismically active East Agri (EAFS) and Monti della Maddalena (MMFS) extensional fault systems. The reservoir rocks are sealed and separated from shallower thrust sheets by a clay-rich and overpressured mélange. The role of this mélange during fault evolution at shallow crustal levels is widely debated and perhaps underestimated. Here, through multi-scale structural analyses and U–Pb dating of syn-tectonic calcite mineralizations, we gain new insights into the Val d'Agri fault system architecture, their structural maturity, and their relations with both natural and induced seismicity. Consistent with present-day NE-SW crustal stretching, the macro-scale structural architecture of both EAFS and MMFS is controlled by NW-SE and NE-SW fault sets, which displaced and in part re-sheared inherited pre- and syn-orogenic structures. The lack of evident clustering of meso-scale faults and the radial pattern of related slickenlines suggest that polygonal-like faulting occurred, particularly along the EAFS, due to lateral spreading of the Irpinia mélange in the subsurface. Structural data show that the MMFS is characterized by a higher structural maturity (slip longevity), with calcite U–Pb ages indicating the onset of long-lasting extensional tectonics in Early-Middle Miocene time. The original results are discussed in terms of seismotectonic setting of the study area, emphasizing the role played by both the thickness and spatial distribution of plastic mélange in modulating fluid pressure and seismic faulting.

1. Introduction

Faults can act as conduits, barriers, or conduit-barrier systems for fluids, such as hydrocarbons, groundwater, and geothermal solutions, promoting their accumulation or leakage into or out from reservoirs (e. g., Caine et al., 1996; Sibson 2020). In addition to seismic analyses and numerical modelling, detailed structural characterization at different scales of exposed faults is required to identify their influence on the integrity of deep reservoirs and on the fluid storage and migration properties of fractured reservoirs (e.g., Peacock and Sanderson, 2018; Smeraglia et al., 2021). Moreover, useful information regarding fault length, downdip rupture length, bottomset depth, and structural maturity can be obtained with relevant implications for seismic hazard assessment (Wells and Coppersmith, 1994; Cello, 2000; Manighetti et al., 2007; Leonard, 2010; Bello et al., 2022).

Here, we study the intermontane Val d'Agri Basin, located in the southern Apennine fold-thrust belt (Italy). This basin is characterized by high seismic hazard, as demonstrated by the 1857 Mw 7.1 earthquake and several historical and instrumental earthquakes of lower magnitude (Mallet, 1862; CPTI, 2022). In addition to natural seismicity, induced seismic events linked to industrial activities recently occurred in the basin (Valoroso et al., 2009; Stabile et al., 2014, 2021; Improta et al., 2017; Rinaldi et al., 2020; Hager et al., 2021; Picozzi et al., 2022). The basin hosts the largest onshore oil field in western Europe, producing hydrocarbons since 1993, with a current production of 10,000 m^3 d^{-1} of oil and 4,000,000 m^3 d^{-1} of gas (Hager et al., 2021). Despite its

---

economic importance, the geometry, kinematics, and location of main seismic structures (e.g., Benedetti et al., 1998; Cello et al., 2003; Maschio et al., 2005; Improta et al., 2010; Bello et al., 2022), as well as the tectonic architecture and evolution of the basin (Monaco et al., 1998; Cello et al., 2000; Giano et al., 2000; Maschio et al., 2005; Barchi et al., 2007; Zembo et al., 2009, 2011; Brozzetti, 2011; Candela et al., 2015; D'Adda et al., 2017) are still debated.

We present a multidisciplinary study on exposed faults, including field structural analysis, geometrical and kinematic fault analysis, multiscale fault length distribution, microstuctural analyses, and calcite U–Pb dating. In particular, we focus on the assessment of the large-scale structural architecture of the study area in order to decipher the tectonic evolution of the basin and the possible relations between exposed extensional-transtensional faults and sources of natural and induced seismicity. The fault pattern in the Val d'Agri Basin is very complex and has been explained through various tectonic evolutionary models. Our data improve and advance these previous models by providing evidence for deformation processes hitherto not described in the study area, such as re-activation of the pre-orogenic forebulge extensional faults (Doglioni, 1995; Vitale et al., 2012; Tavani et al., 2023) and polygonal-like faulting (i.e., layer-bound normal faults arranged in polygonal patterns and multi-direction strikes; Xia et al., 2022). These results may be useful for the exploitation of natural fluids and the mitigation of seismic hazard.

2. Geological and structural settings

2.1. Southern Apennines

The southern Apennines are the result of the collision and interaction between the African and Eurasian plates and the intervening Adriatic or Adria microplate (e.g., Malinverno and Ryan, 1986; Carminati and Doglioni, 2012). Since the Oligocene, westward-directed oceanic subduction beneath the European plate and, later, the early stage of continental collision between Adria and Europe caused NNE-SSW oriented shortening and formed the Apennine accretionary wedge (e.g., Hippolyte et al., 1994; Scrocca et al., 2005).

NE-verging thrusting produced a complex nappe stack, characterized, from top to bottom, by the superposition of the following paleogeographic domains. Eocene (?)-Miocene wedge top basin deposits (Fig. 1b), comprising the Gorgoglione Fm., lay unconformably above the Albidona Fm. (Fig. 2), which is controversially interpreted as syn-orogenic sediments deposited during (Lentini et al., 1987; Cello and

Mazzoli, 1998) or before (Patacca and Scandone 2007; Prosser et al., 2021) the contractional deformation of Adria paleomargin. The Ligurian Accretionary Complex is mainly formed by deep-sea sedimentary and metamorphic rocks (Fig. 1b and 2), which originated from west-directed subduction of the oceanic crust originally located between the Adria and the European plates (Patacca and Scandone, 2007; Prosser et al., 2021). The Adria passive margin, from west to east, includes the Apennine Carbonate Platform, consisting of a thick succession of shallow water carbonates of Triassic to Miocene age; the Lagonegro Basin, consisting of proximal to distal pelagic successions of Triassic to Miocene age; and the Apulian Carbonate Platform, made of a thick succession of shallow water carbonates of Triassic to Miocene age (Roure et al., 1991; Monaco et al., 1998; Patacca and Scandone, 2007, Fig. 1b and 2). The Lagonegro Basin is deformed into two major thrust sheets: Lagonegro I and Lagonegro II. These override the underlying Apulian Carbonate Platform along a regional décollement layer (i.e., Irpinia mélange; Roure et al., 1991; Mazzoli et al., 2001; Patacca and Scandone, 2007, Fig. 2b). This decollement layer consists of low permeability (k < 10−7 mD), intensely deformed and overpressured deep-water clay-rich mudstone and siltstones of Miocene to Lower Pliocene age (Mazzoli et al., 2001; Hager et al., 2021). The Irpinia mélange thickness is particularly heterogeneous. Generally, it is several hundreds of meters thick (Butler et al., 2004), with a tendency to thin toward SW and NW (Butler et al., 2004; Catalano et al., 2004; Ascione et al., 2013; Mazzoli et al., 2014; Antoncecchi, 2020; Rinaldi et al., 2020); however, locally, it can be as thick as 2 km, in correspondence of the Val d'Agri oilfield (Hager et al., 2021).

The transition from mainly thin-to partly thick-skinned contractional deformation has occurred since Pliocene time (e.g., Butler et al., 2004; Corrado et al., 2005; Mazzoli et al., 2008). The activation of deep and steep reverse faults triggered, at shallow crustal levels, syn-contractional gravitational collapses of the wedge along low-angle normal faults (e.g., Bucci et al., 2014; Mazzoli et al., 2014). In early Pleistocene time, the eastward foreland-directed thrust migration was inhibited by the thickening of the colliding continental lithosphere (Doglioni et al., 1994); consequently, strike-slip tectonics became predominant (e.g., Hippolyte et al., 1994). In Middle-Late Pleistocene time, coeval with the opening of the Tyrrhenian Sea back-arc basin, tectonics switched from compressional/strike-slip to extensional, with a NE-SW direction of stretching that is still active (Mariucci and Montone, 2020). Extensional tectonics progressively migrated eastward (i.e., foreland-ward) and presently affect the axial zone of the southern Apennines. Toward the east, the Bradano foredeep marks the presently active frontal part of the
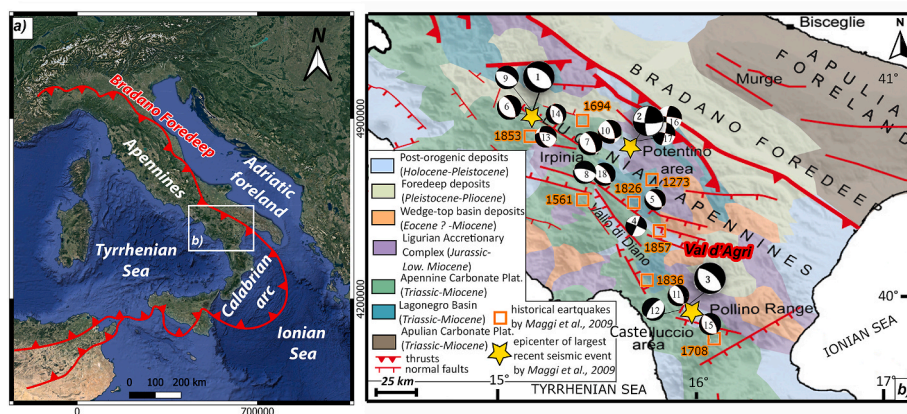

Fig. 1. a) Map of the Apennines subduction front and location of panel-b (white rectangle). b) Structural map of the southern Apennines: different background colors show the tectonic units (modified by Vezzani et al., 2010; Vitale and Ciarcia, 2018); orange squares: historical earthquakes with intensity > VIII (Maggi et al., 2009); yellow stars: epicenters with focal mechanisms of the three most recent and largest events (1-Irpinia area, 1980, Mw 6.9, depth 10 km; 2- Potentino area, 1990, Mw 5.7, depth 26 km; 3-Castelluccio area, 1998, Mw 5.6, depth 10 km; Cucci et al., 2004; Maggi et al., 2009). Also, the focal mechanisms of Mw > 4.5 earthquakes between 1971 and 2023 in the southern Apennines are shown (Cucci et al., 2004; Pondrelli et al., 2020; Table S1). (For interpretation of the references to color in this figure legend, the reader is referred to the Web version of this article.)
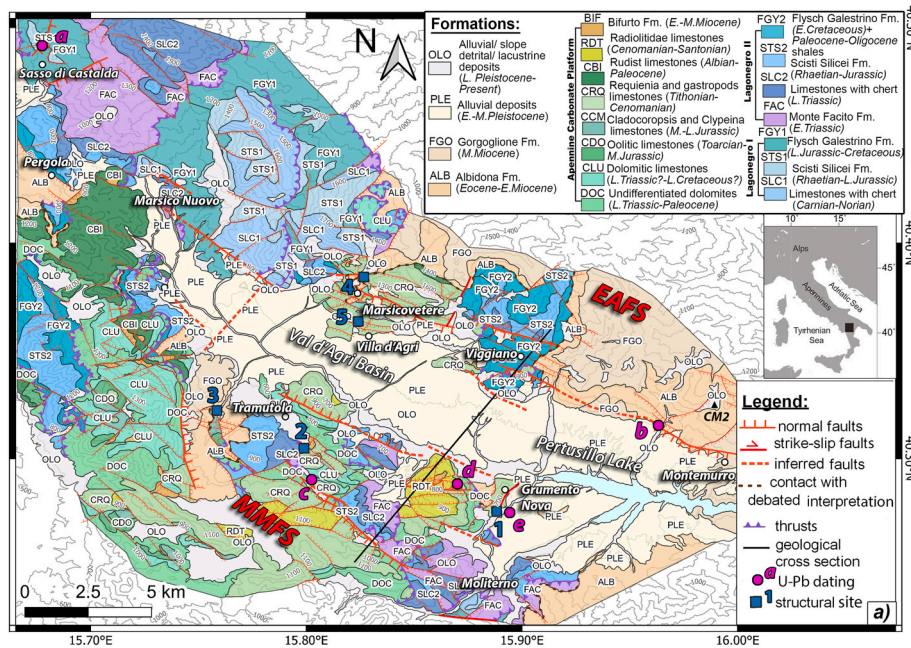
Fig. 2. a) Geological-structural map of the Val d'Agri Basin (EAFS: East Agri Fault System; MMFS: Monti della Maddalena Fault System) showing: sites of structural analysis (blue squares); sites of U–Pb dating (pink circles); and trace of the geological section shown in panel b. b) Geological cross-section. Deep structure geometry was drawn following the seismic line interpretation of Mazzoli et al. (2013), Candela et al. (2015), and well stratigraphy reported in Antoncecchi (2020). Shallow structures are based on surface geology displayed in panel a. (For interpretation of the references to color in this figure legend, the reader is referred to the Web version of this article.)

orogenic belt (e.g., Montone et al., 2004; Ferranti et al., 2009, Fig. 1a).

2.2. Val d'Agri Basin

The Val d'Agri Basin (Fig. 1b) is bounded by two post-orogenic extensional-transtensional high-angle fault systems: the SW-dipping East Agri Fault System (EAFS; Fig. 2a) located along the north-eastern side of the valley, and the NE-dipping Monti della Maddalena Fault System (MMFS; Fig. 2a) located along the western side (Cello et al., 2000; Maschio et al., 2005). Additionally, outcropping faults with different attitudes were previously recognized and associated with the polyphasic tectonic evolution of the basin (Cello et al., 2000; Giano et al., 2000; Bucci et al., 2012; Candela et al., 2015). The origin of the Val d'Agri Basin and, in particular, the role of the EAFS and/or MMFS is still debated in the literature. A first model suggested a late-orogenic strike-slip origin and predominant left-lateral kinematics for the EAFS faults; these high-angle faults dissected and, in part, reactivated inherited Late Miocene-Early Pleistocene NNW-SSE-striking flat and ramp thrusts (e.g., Monaco et al., 1998; Cello et al., 2000). A second model proposed that the late orogenic strike-slip activity of the EAFS faults was followed by their dip-slip extensional reactivation during post-orogenic extension (e.g., Giano et al., 2000; Barchi et al., 2007). A third and more recent model envisioned that late-orogenic strike-slip activity of the EAFS faults was followed by the extensional activation of

the NW-SE-striking MMFS high-angle faults during post-orogenic extension, which generated an asymmetric opening of the Val d'Agri Basin, and consequently triggered the extensional reactivation of the EAFS (e.g., Maschio et al., 2005; Zembo et al., 2009, 2011; Brozzetti, 2011).

The structural architecture of the Val d'Agri Basin is further complicated by the controversial role of the Irpinia mélange. Indeed, some authors proposed the complete decoupling between structures located within the Apulian Carbonate Platform and those located within the allochthonous units (D'Adda et al., 2017; Hager et al., 2021). Others assessed a potential soft linkage (Borraccini et al., 2002; Candela et al., 2015), or possible hard structural connections cutting through the mélange (Barchi et al., 2007; Brozzetti, 2011; Rinaldi et al., 2020; Valoroso et al., 2023).

Recent tectonic activity of the MMFS and EAFS is supported by the results of paleoseismological analyses, which documented active faulting between 40 and 20 ka along the EAFS (Giano et al., 2000), and between 20 and 0.6 ka along the MMFS (Improta et al., 2010). Furthermore, historical and instrumental earthquakes occurred in the Val d'Agri Basin, such as the 1857 destructive event (Mw 7.1; Mallet, 1862, Fig. 1b). The debate concerning the nature, location, and attitude of seismogenic fault(s) in the area is still open (e.g., Benedetti et al., 1998; Cello et al., 2003; Maschio et al., 2005; Improta et al., 2010; Bello et al., 2022).

In the last decades, low to moderate instrumental seismicity has been recorded in the Val d'Agri Basin area (Cucci et al., 2004; Improta et al., 2010, 2017; Maschio et al., 2005; Maggi et al., 2009). In addition, this area is also affected by induced microseismicity related to industrial activities. In particular, low-magnitude events that occurred beneath the southern part of the artificial Pertusillo lake (Fig. 2a) were related to both loading-unloading effects related to seasonal changes in lake water level (2003–2005 swarm; Valoroso et al., 2009; Stabile et al., 2014; Improta et al., 2017; Rinaldi et al., 2020; Picozzi et al., 2022), and to a combination of water level oscillations with the regional tectonics (2013–2015 swarm; Picozzi et al., 2022). Furthermore, since 2006, microseismicity has often occurred due to wastewater reinjection at the Costa Molina 2 (CM2) hydrocarbon well (Fig. 2a; Improta et al., 2017; Hager et al., 2021; Stabile et al., 2021).

3. Methods

We conducted field data collection using the FieldMove App on an Apple iPad to gain structural data such as the attitude of faults and related slip (striae, slickenfibres). For every ten measurements, we checked the reliability of digital measurements by comparing them with those obtained with an analog compass. We classified as meso-scale faults all measured faults with a lateral continuity longer than 10 m (Table S2).

Using QGIS software, we produced a structural-geological map (Fig. 2a) integrating our original fieldwork and previous maps by Carbone et al. (1991), Bucci et al. (2012), and Antoncecchi (2020), Palladino et al. (2023) Foglio 505 "Moliterno" and Foglio 489 "Marsico Nuovo" (ISPRA, https://www.isprambiente.gov.it/Media/carg/505_MOLITERNO/Foglio.html; https://www.isprambiente.gov.it/Media/carg/489_MARSICO_NUOVO/Foglio.html). Exhumed normal and strike-slip faults with a length >200 m were classified as "macro-scale faults" (Table S2). We classified as "inferred" buried faults representing the lateral prolongation of macro-scale faults and those deduced by seismic studies (e.g., Borraccini et al., 2002; Valoroso et al., 2009; Improta et al., 2017).

The analysis of fault geometry and kinematics on both macro- and meso-scale faults was performed using Stereonet and FaultKin software (https://rickallmendinger.net). We calculated the trend of macro-scale faults by using the NetworkGT plugin in QGIS software (Nyberg et al., 2018). To identify the fault sets, we plotted both macro-scale fault trends and meso-scale fault strikes through rose diagrams (bin size 10°) in Schmidt projections (lower hemisphere). To assess the fault kinematics, we plotted the attitudes of meso-scale slip surfaces, slickensides, and striae.

We performed a multiscale length analysis of macro-scale faults to evaluate the degree of structural maturity of both EAFS and MMFS. After topological artifact corrections, we automatically calculated the fault lengths (L) by NetworkGT QGIS plugin (Nyberg et al., 2018). Then, using the Excel software, we plotted the lengths of macro-scale faults as a function of their cumulative number (N) in a log-log space and computed both exponential (Equation (1)) and power law (Equation (2)) best fit distributions using, respectively:

$$N(L) = \alpha \; e^{-\alpha L} \tag{1}$$

$$N(L) = m^* \; L^{-D} \tag{2}$$

Where m is the proportionality coefficient for scaling law, D is the fractal dimension, and α is the exponent of negative exponential distribution (Bonnet et al., 2001; Ceccato et al., 2022). We calculated the regression lines and the associated coefficient (i.e., R^2) by applying Equations (1) and (2) to our original dataset. The D value, i.e., the slope of the power-law regression line, was employed to evaluate the degree of structural maturity of EAFS and MMFS fault systems and single fault sets. The structural maturity indicates the slip longevity of a fault, depending on the fault initiation age, total cumulative slip, length, and

slip rate (e.g., Manighetti et al., 2007, 2021). Considering that known fault populations have D values between 0.7 and 2, low D values are associated with limited structural maturity, whereas high D values correspond to high structural maturity (Cladouhos and Marrett, 1996; Spyropoulos et al., 1999; Cello, 2000; Bonnet et al., 2001; Marchegiani et al., 2006).

We performed microstructural analyses on nine thin sections from fault rocks by optical and cathodoluminescence (CL; operated at 15 kV and 250 μA beam current) microscopy at Sapienza University of Rome and ETH Zurich to identify different events of crystal growth/deformation. On seven additional thin sections (80 μm thick) from slickenfibers sampled along differently oriented slickensides (Table S3, Fig. 1), we attempted carbonate U–Pb dating at ETH Zurich by laser ablation inductively coupled plasma mass spectrometry (LA-ICP-MS). Due to the low U–Pb ratios and/or element remobilizations in association with later slip events occurred along single faults (Table S3), only two sections yielded reliable U–Pb ages. Analytical methods and correction procedures followed Roberts et al. (2017) and Guillong et al. (2020). We calculated U–Pb ages from Tera-Wasserburg concordia lower intercepts using the IsoplotR software package (Vermeesch, 2018). All uncertainties are reported at the 95% confidence level.

4. Results

4.1. Fault geometry and kinematics analyses

At the regional scale, both EAFS and MMFS are segmented (Fig. 2a and 3) and constituted by faults with variable attitudes. In both fault systems, the macro-scale faults form two main high-angle fault sets, respectively trending NW-SE and NE-SW (Fig. 3). The former is the most frequent and includes fault traces trending ca. N125° (±15°) in the EAFS, and ca. N135° (±15°) in the MMFS. The latter includes fault traces trending ca. N55° (±15°) in both fault systems (plots 1 and 3 in Fig. 3).

At the local scale, EAFS and MMFS display considerable differences (Fig. 3). In the EAFS, the meso-scale faults (plots 2 and 3 of Fig. 3) show a not-to poorly-systematic distribution. Moreover, the attitude of macro- and meso-scale faults differs (plots 1 and 2 in Fig. 3). For instance, the NW-SE trend is frequent in the macro-scale faults but much less frequent at the meso-scale. The NE-SW-trending faults, which are well clustered in the macro-scale population, show a wide range of strike directions spanning between N20° and N70° in the meso-scale population (plot 2 in Fig. 3). We also note that the meso-scale population is characterized by numerous N–S-striking high-angle faults, which are absent in the macro-scale population. On the contrary, in the MMFS the orientation of macro- and meso-scale faults is similar (plots 5 and 6 in Fig. 3 and plot 4 in Fig. 3). In particular, the NE-SW and NW-SE sets are present at all scales, and at the meso-scale they are mainly characterized by steep faults (i.e., dip angles 60°–90°; plot 6 in Fig. 3). However, we note that the meso-scale NNE-SSW striking faults are not present in the macro-scale population (plots 4 and 5 in Fig. 3).

The slip attitudes of the EAFS faults exhibit an outward radial pattern (Fig. 4a), whereas within the MMFS fault population, two main slip directions, namely toward NE-SW and NW-SE, are recognizable over a background radial pattern. (Fig. 4b). In the MMFS meso-scale faults, the NE-SW striking set shows normal to mainly dextral transtensional kinematics, whereas the NW-SE striking set shows normal to dextral transtensional kinematics with minor evidence of left-lateral kinematics (Fig. 4b).

4.2. Fault length analysis

To evaluate the structural maturity of the fault system, we carried out a length analysis of macro-scale faults (Fig. 5). The exponential law provided a fit with a $R^2 \geq 0.98$ for both EAFS and MMFS, whereas the power law provided a fit of $R^2 = 0.92$ and $R^2 = 0.84$ for the EAFS and the MMFS, respectively. This fitting could be due to the gradual transition
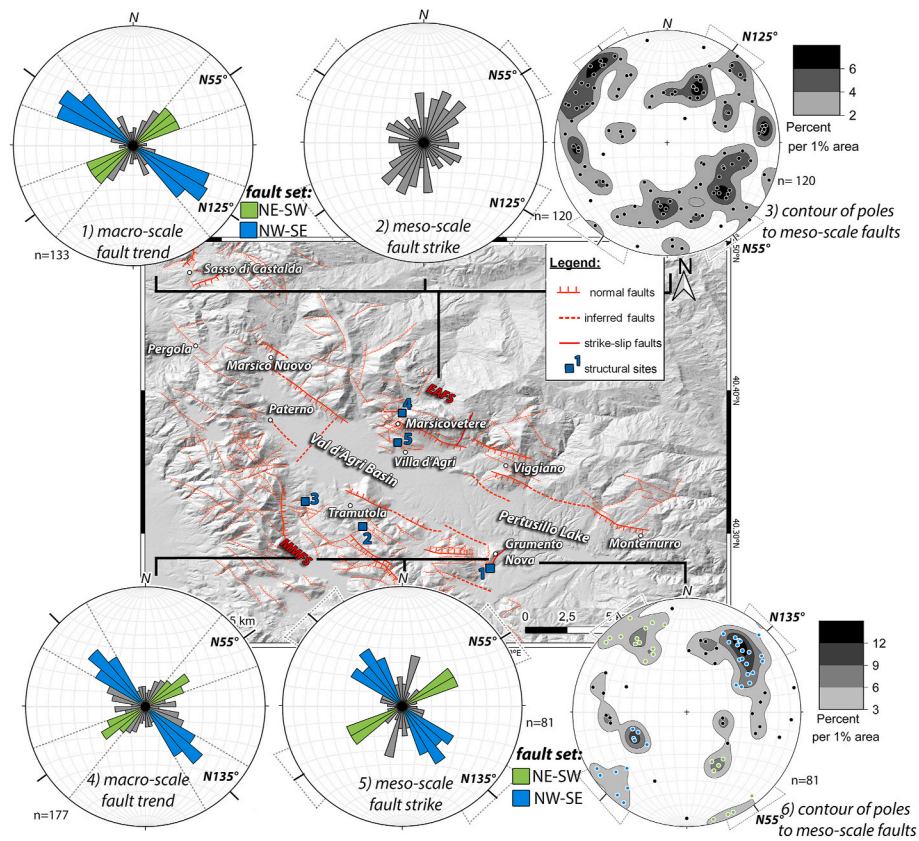
Fig. 3. Structural map on digital terrain model by TINITALY (10 m resolution; Tarquini et al., 2007) with Schmidt projections (lower hemisphere) and rose diagrams (bin size 10°) for macro- and meso-scale faults from EAFS (above) and MMFS (below). Plots 1 and 4 show strike azimuths of macro-scale faults, with NE-SW and NW-SE sets in green and blue, respectively. Dotted black lines are the azimuth boundaries of fault sets. Plots 2 and 5 show strike azimuths of meso-scale faults. In plot 5, the NE-SW and NW-SE striking sets have the same colors as the macro-scale faults. Plots 3 and 6 show contours to fault poles. In plot 6, poles to NE-SW and NW-SE striking faults have the same colors as the macro-scale faults. In all plots, n is the number of analyzed faults. (For interpretation of the references to color in this figure legend, the reader is referred to the Web version of this article.)
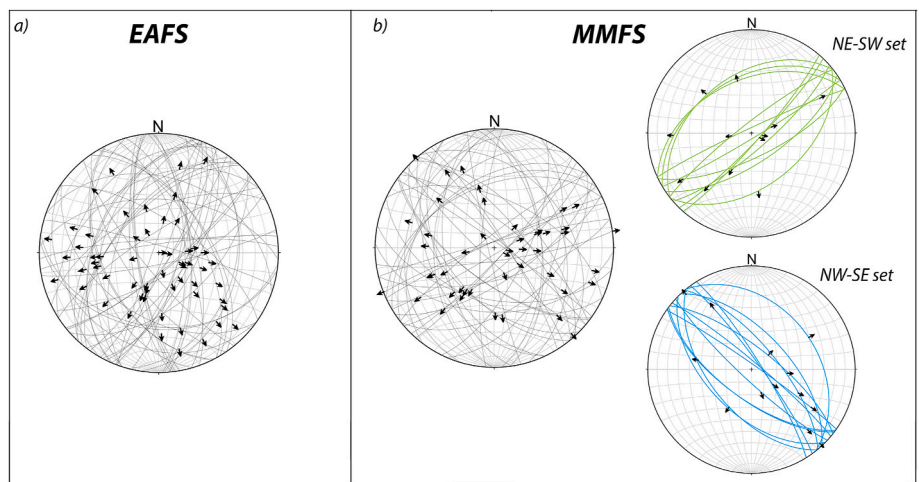

Fig. 4. Schmidt projections (lower hemisphere) showing attitude of meso-scale fault planes and striae from the EAFS (panel a) and MMFS (panel b). Panel b also shows the attitude of NE-SW and NW-SE striking faults (green and blue, respectively) and related striae. (For interpretation of the references to color in this figure legend, the reader is referred to the Web version of this article.)

from power law to exponential distribution of fault lengths with the increase of strain (Bonnet et al., 2001) and/or to resolution issues related to underrepresentation of shortest (truncation) and longest (censoring) faults (Ortega et al., 2006). However, assuming a self-organized critical system by fitting the power law (Spyropoulos et al., 1999), fault growth can be studied as a fractal process as widely documented in the literature (e.g., Cladouhos and Marrett, 1996; Bonnet et al., 2001; Ceccato et al., 2022). Excluding data interpreted as truncation or censoring artifacts (empty dots in Fig. 5a–c), we computed a good best fit for power-law regression ($R^2 > 0.8$). In this way, the obtained D values of 0.96 and 1.19 for the EAFS and MMFS, respectively, are employed to evaluate the structural maturity of the studied fault
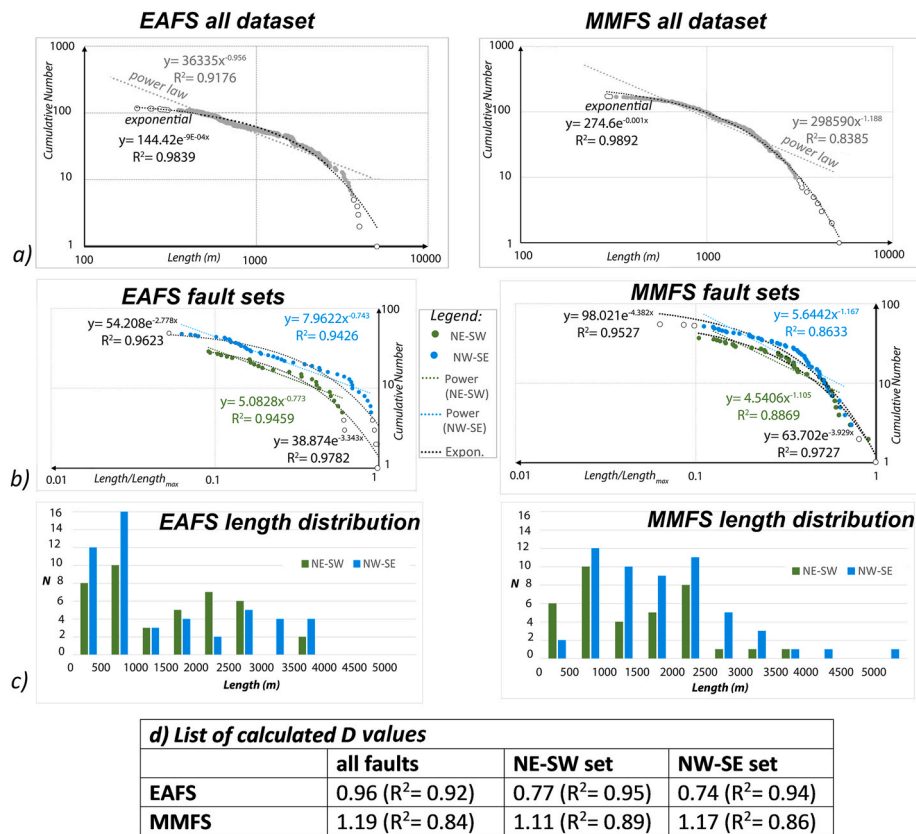
Fig. 5. Fractal analyses of fault segments from the EAFS and MMFS. a) Log-log diagram of cumulative number vs. fault length for macro-scale faults. The best fit lines for power law and exponential regressions are dashed in grey and black, respectively. R^2 is the coefficient of regression. The empty dots are the data excluded from the power law (see text for details). b) Log-log diagram of cumulative number vs. fault normalized length (i.e., fault length to maximum fault length ratio) for NE-SW (green dots) and NW-SE (blue dots) fault sets of EAFS and MMFS. The best fit lines for power law and exponential regressions are dashed, colored, and black, respectively. The empty dots are the data excluded from power law (same reason as above) c) Histograms showing fault length distribution for the NE-SW and NW-SE fault sets of EAFS and MMFS. d) List of D values and related R^2, calculated from power law regressions reported in panels a and b. (For interpretation of the references to color in this figure legend, the reader is referred to the Web version of this article.)

systems. Accordingly, a higher structural maturity degree is assessed for the MMFS relative to the EAFS.

Additionally, we perform fractal analysis, separating data associated with the NE-SW fault set from those of the NW-SE fault set. In order to compare data acquired for fault sets pertaining to the two fault systems, we normalized the values of fault length by dividing the single values by the maximum fault length value. As a consequence, we compute a D value of 0.77 and 0.74, respectively, for the NE-SW and NW-SE sets pertaining to the EAFS and a D value of 1.11 and 1.17, respectively, for the NE-SW and NW-SE sets of the MMFS. We note that the EAFS sets have D values smaller than those of the entire fault population, whereas the D values for the MMFS sets are nearly equal to those of the entire fault population (Fig. 5c).

We also analyze the length frequency of the two aforementioned sets (NE-SW and NW-SE; Fig. 5c). For both fault systems, the NW-SE set is more frequent and longer than the NE-SW one. In the EAFS, the NW-SE faults have a maximum length of c. a. 4 km, whereas in the MMFS, they reach a maximum length of c. a. 5 km. In the MMFS, the frequency of NE-SW faults significantly decreases as length increases. The same effect is less evident in the EAFS.

4.3. Crosscutting relations

We analyze five areas with clear exposures to determine crosscutting relations among faults (Fig. 2). Site 1 (Fig. 2; 40°16′32″N, 15°53′22″E) is located along the MMFS and exposes Lower Cretaceous limestones of the Apennine Carbonate Platform (CRQ; Fig. 2) displaced by a S-dipping and

E-W-striking normal fault with less than 50 m-throw (yellow fault in Fig. 6a). This fault also cuts and displaces a high-angle, NNE-SSW-striking, left-lateral fault (orange fault in Fig. 6a). At the same locality (Fig. 6b), we also observe that NNE-SSW-striking slip surfaces show both left- and right-oblique transtensional kinematics (orange plot). Instead, the E-W-striking slip surfaces are characterized by pronounced strike direction variability (from E-W to NW-SE; yellow plot). In places, the E-W-striking surfaces are cut by high-angle NW-SE-striking normal to transtensional faults (blue plot; Fig. 6b). All slip surfaces are coated by calcite slickenfibers. Micro-structural analyses show that the slickenfibers include blocky calcite and multiple slip surfaces, consistent with several phases of fault activity (Fig. 6c, d, 6e).

Site 2 (Fig. 2; 40°18′17″N, 15°48′00″E) is located along the MMFS, south of the Tramutola village. There, the Lower Cretaceous limestones of the Apennine Carbonate Platform (CRQ; Fig. 2) are displaced by a high-angle, NW-SE-striking normal fault with less than 50 m-throw (blue fault in Fig. 7a). This fault displaces a NE-SW-striking normal fault that is partly a reactivation of a 20°-dipping pre-existing thrust fault (green fault in Fig. 7b).

Site 3 (Fig. 2; 40°19′23″N, 15°45′29″E) is located along the MMFS (Fig. 8a). There, an E-W-striking right-lateral fault (yellow fault in Fig. 8a) juxtaposes the Albidona Fm. in the hanging wall against the Middle-Late Jurassic Apennine Carbonate Platform limestones in the footwall (CCM; Fig. 2). The fault displaces by ca. 25 m a N–S-striking extensional fault (purple fault within the plot of Fig. 8a), whose main slip surface is coated by reddish slickensides (Fig. 8b). The fault rock consists of a cataclasite close to the slip surface and a proto-cataclasite
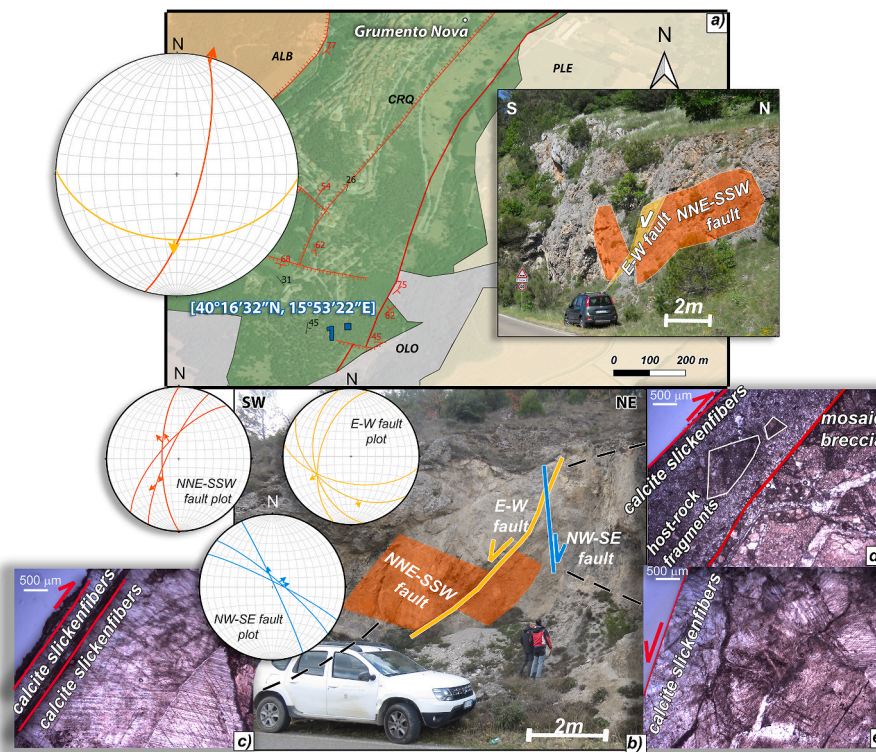
Fig. 6. a) Close-up view of Fig. 2 showing structural site 1, related outcrop, and Schmidt projections (lower hemisphere) indicating an E-W-striking normal fault (yellow) that displaces a NNE-SSW-striking left-lateral fault (orange). The outcropping formations are: Tithonian-Cenomanian Requienia and gastropods limestones (CRQ), Eocene-Early Miocene Albidona Fm. (ALB), Early-Middle Pleistocene alluvial deposits (PLE), and Late Pleistocene-Present alluvial/slope detrital/lacustrine deposits (OLO). b) Outcrop and Schmidt projections (lower hemisphere) of minor faults associated with these faults. The image shows a high-angle NW-SE-striking normal to transtensional fault (blue) that displaces an E-W-striking normal fault (yellow) that, in turn, displaces a NNE-SSW-striking normal to transtensional fault (orange). c) d) and e) Optical microscopy images (parallel light) of slickenfibers sampled along the fault surfaces shown in Fig. 5b, as indicated by the dashed lines. Red lines represent slip surfaces, and red arrows represent slip directions and sense of motion. (For interpretation of the references to color in this figure legend, the reader is referred to the Web version of this article.)

far from it (Fig. 8c and d).

Site 4 (Fig. 2; 40°23′03″N, 15°49′38″E) is located along the EAFS, to the north of the Marsicovetere village. This is shown in the northwestern part of Fig. 9a, where an E-W-striking normal fault displaces a N–S-striking fault (Fig. 9b). The E-W-striking fault includes two splays showing a cumulative displacement of about 100 m and juxtaposing the Albidona Fm. in the hanging wall (Fig. 2) against the Lower Cretaceous Apennine Carbonate Platform limestones in the footwall (CRQ; Fig. 2). The N–S-striking slip surface is coated by reddish slickensides (Fig. 9c and d), showing both normal and right-lateral kinematics (purple fault within the plot of Fig. 9b). The fault-related mineralization includes a mosaic breccia characterized by different slip surfaces, supporting the occurrence of multiple phases of activity (Fig. 9e).

Toward the east, the Lower Cretaceous Apennine Carbonate Platform limestones (CRQ; Fig. 2) are displaced by a NW-SE-striking fault, which offsets multiple NE-SW-striking left-lateral transtensional fault segments (Fig. 9f). The NW-SE fault surface is coated by calcite slickenfibers indicating right-lateral transtensional kinematics, hence suggesting multiple phases of activity (blue fault within the plot of Fig. 9f). The slickenfibers are very thin, and the fault rock consists of a proto-cataclasite with survivor grains in contact with each other (Fig. 9g and h). The NE-SW-striking fault splays include reddish slickensides consistent with right-lateral transtensional kinematics (green fault within the plot of Fig. 9f and i). The fault rock also consists of proto-cataclasite crosscut by multiple slip surfaces, which suggests multiple phases of activity (Fig. 9k).

Site 5 (Fig. 2; 40°21′50″N, 15°49′23″E) is located along the EAFS, to the north of the Villa d'Agri village (Fig. 7c). There, the Triassic dolomites (DOC; Fig. 2) and Lower Cretaceous limestones (CRQ; Fig. 2) of the

Apennine Carbonate Platform limestones are dissected by a NW-SE-striking normal fault (blue fault within the plot of Fig. 7c), also displacing a NE-SW-striking normal fault (green fault; Fig. 7g). The latter fault, in turn, displaces a low-angle E-W-striking normal fault (yellow fault; Fig. 7d). The NW-SE- and the NE-SE-striking faults are characterized by throws of c. a. 50 and > 150 m, respectively. The NE-SW-striking fault rock consists of proto-to cataclasite (Fig. 7h), whereas the E-W-striking fault rock is crosscut by several slip surfaces that separate gouge, chaotic breccia, and cataclasite (Fig. 7e and f).

4.4. Calcite U–Pb dating

We were able to constrain the time frame of activity of two faults near structural sites 1 and 2 using calcite U–Pb geochronology (Fig. 2a). The first U–Pb age is from slickenfibres coating a high-angle NW-SE-striking right-lateral transtensional fault with a lateral continuity <10 m, exposed to the south of Tramutola village in the Monte Aquila area (40°17′25″N 15°48′16″E; Fig. 10a and c). The dated fault is a splay structure of a NNW-SSE-striking normal fault (Fig. 10b), which is cut by the main NW-SE-striking Monte Aquila Fault (Fig. 10a). This latter fault juxtaposes Calcari Dolomitici (CLU) in the hanging wall against Dolomie Indifferenziate (DOC; Fig. 2a). The dated fibers are composed of blocky calcite crosscut by microscale shear fractures (Fig. 10d). In particular, we note that the blocky crystals, dated to 13.50 ± 2.47 Ma (Miocene; Fig. 10e), are crosscut by a second generation of slickenfibers with smaller crystals (Fig. 10d).

The second U–Pb age is from calcite slickenfibres from a high-angle NE-SW-striking right transtensional fault, exposed in a quarry a few kilometers west of the Grumento Nova village (40°17′19″N, 15°52′23″E;
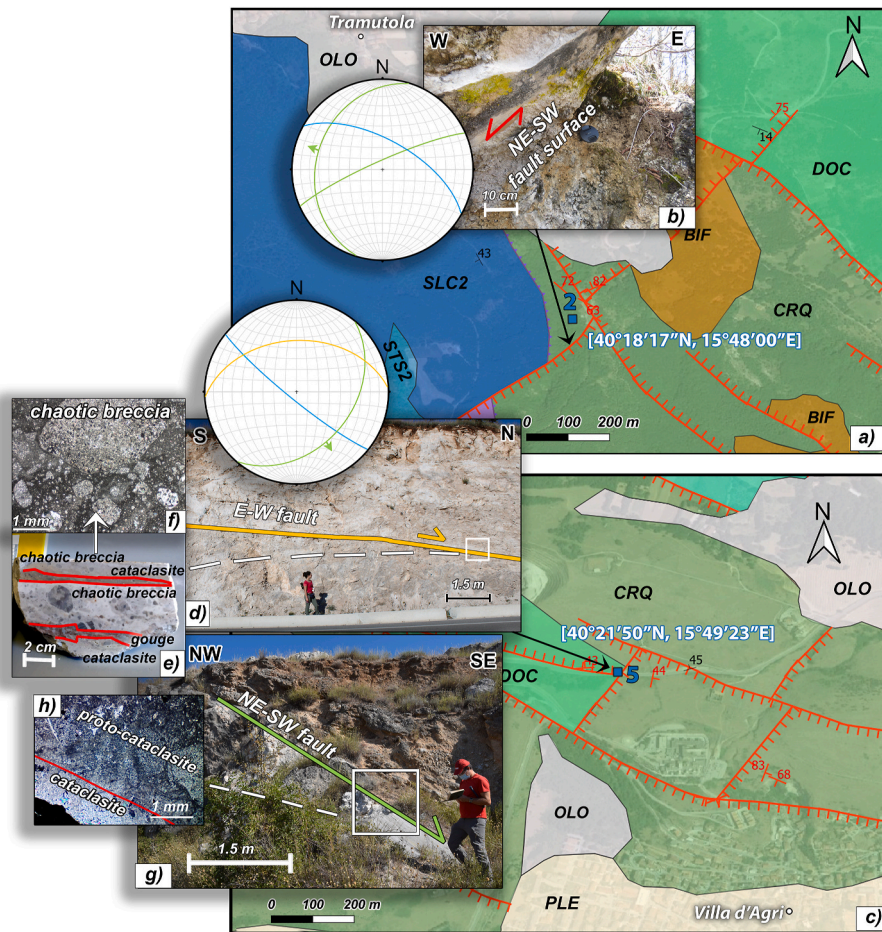
Fig. 7. a) Close-up view from Fig. 2 showing structural site 2 (40°18′17″N, 15°48′00″E), related outcrop, and Schmidt projections (lower hemisphere). The outcropping formations are: Late Triassic limestones with flint (SLC2), Rhaetian-Cretaceous Scisti Silicei Fm. (STS2), Late Triassic-Paleocene undifferentiated dolomites (DOC), Tithonian-Cenomanian Requienia and gastropods limestones (CRQ), Early-Middle Miocene Bifurto Fm. (BIF), and Late Pleistocene-Present Alluvial/slope detrital/lacustrine deposits (OLO). A high-angle NW-SE-striking normal fault (blue) that displaces a NE-SW-striking normal fault (green) is shown. b) Detail of the NE-SW-striking fault surface exposed in the footwall of the NW-SE-striking fault. Here the fault strike is partially rotated to N–S (low-angle green plane in the Schmidt projections). The red arrow represents the slip direction and sense of motion. c) Close-up view from Fig. 2 showing structural site 5 (40°21′50″N, 15°49′23″E), related outcrop, and Schmidt projections. The outcropping formations are: Late Triassic-Paleocene undifferentiated dolomites (DOC), Tithonian-Cenomanian Requienia and gastropods limestones (CRQ), Early-Middle Pleistocene alluvial deposits (PLE), and Late Pleistocene-Present alluvial/slope detrital/lacustrine deposits (OLO). A high-angle NW-SE-striking normal fault (blue in the figure) that displaces a NE-SW-striking normal fault (green) that, in turn, displaces a low-angle E-W-striking normal fault (yellow) is shown. d) Exposure of the low-angle E-W-striking fault. e) Rock slab from the core of the low-angle E-W-striking fault. f) Optical microscopy image (cross-polarized light) from the core of the E-W-striking fault. g) Outcrop of the NE-SW-striking fault. h) Optical microscopy image (cross-polarized light) from the core of the NE-SW-striking fault. (For interpretation of the references to color in this figure legend, the reader is referred to the Web version of this article.)

Figs. 2 and 10f). The dated fault is one of many synthetic and antithetic, NE-SW-striking, normal to transtensional faults showing both right- and left-lateral slip components (Fig. 10g), exposed at the hanging wall of the mapped ENE-WSW-striking fault (Fig. 10f). The dated slickenfibres (Fig. 10h) are characterized by blocky calcite (Fig. 10i) in contact with a cataclasite. The U–Pb dating indicates a Pleistocene-Holocene age (0.82 ± 1.28 Ma; Fig. 10l).

5. Discussion

5.1. Structural architecture and polygonal-like faulting

At the macro-scale both EAFS and MMFS include two main fault sets, striking NE-SW and NW-SE, respectively (Fig. 3). However, the results of multi-scale structural analyses reveal the following differences between the two aforementioned fault systems: 1) EAFS exhibits a sharp difference between the macro- and meso-scale structural architectures: meso-scale faults do not show any systematic fault distribution (plots 1 and 2

of Fig. 3), in accordance with the structural architecture of Apennine Carbonate Platform limestones outcropping near Viggiano village (Fig. 2), as described by Abdallah et al. (2023). Differently, MMFS shows similar macro- and meso-scale structural architectures (plots 3 and 4 of Fig. 3). Moreover, EAFS displays an outward radial slip distribution (Fig. 4), whereas MMFS shows two main slip directions over a background radial slip distribution (Fig. 4b). Furthermore, EAFS is characterized by varying D values of the main fault sets with respect to those characterizing the whole macro-scale fault population (0.96 and c. a. 0.75; Fig. 5), whereas MMFS shows nearly similar D values for both the single sets and the entire fault population (c.a. 1.15; Fig. 5).

To explain the data above, we expand on the previous interpretations, highlighting the decoupling role of the Irpinia mélange, which is the overpressured plastic unit forming the regional-scale decollement of the fold-and-thrust belt (Borraccini et al., 2002; Shiner et al., 2004; Ascione et al., 2013; Candela et al., 2015; D'Adda et al., 2017). Accordingly, we propose that a polygonal-like style of faulting occurred above this unit within the competent carbonate rocks cut by
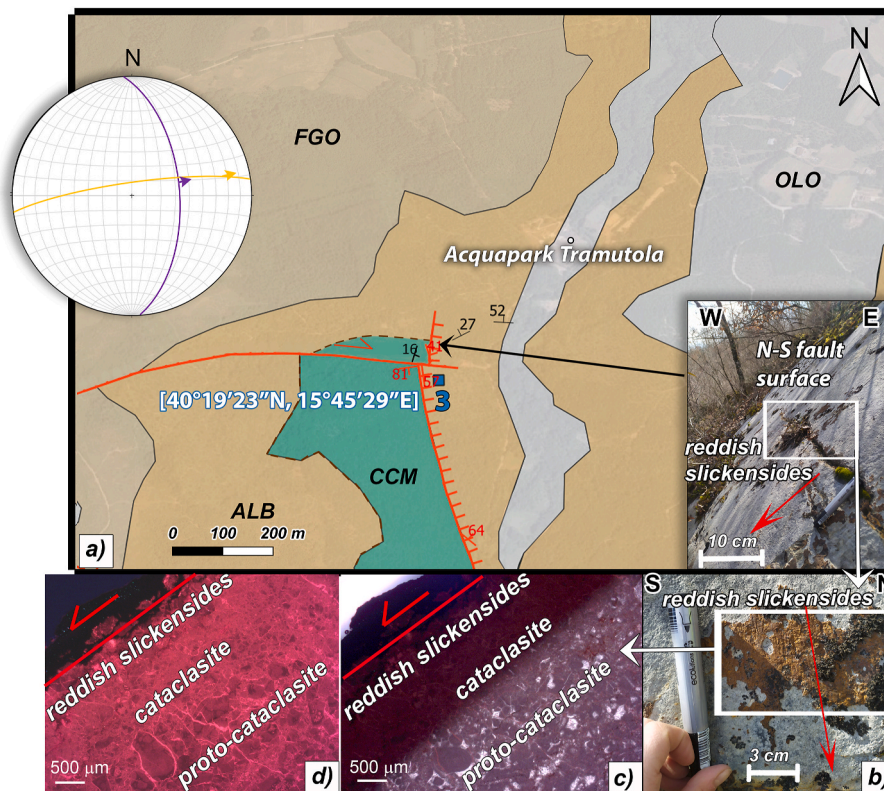
Fig. 8. a) Close-up view from Fig. 2 showing structural site 3 (40°19′23″N, 15°45′29″E), related outcrop, and Schmidt projections (lower hemisphere). The outcropping formations are: Middle-Late Jurassic Cladocoropsis and Clypeina limestones (CCM), Middle Miocene Gorgoglione Fm. (FGO), Eocene-Early Miocene Albidona Fm. (ALB), and Late Pleistocene-Present alluvial/slope detrital/lacustrine deposits (OLO). An E-W-striking normal fault (yellow in the figure) that displaces a N–S-striking normal fault (purple) is shown. b) Detail of a N–S-striking fault surface coated with reddish slickensides. c) Optical microscopy image (parallel Nichols) of reddish slickensides. d) Cathodoluminescence microscopy image of the reddish slickensides. Within all panels, red lines represent slip surfaces, and red arrows indicate slip directions and sense of motion. (For interpretation of the references to color in this figure legend, the reader is referred to the Web version of this article.)

the EAFS. Indeed, the not-systematic orientation of fault strikes and the radial pattern of slip directions documented for the EAFS meso-scale faults are fully consistent with typical features described in well-recognized polygonal fault systems worldwide (e.g., Cartwright, 2011; Elmahdy et al., 2020; Xia et al., 2022). In fact, polygonal faults are often composed of a network of minor normal faults confined to a specific stratigraphic interval by an overpressured and plastic horizon, such as the Irpinia mélange underneath the allochthonous units in the study area, and result in the isotropic collapse of the overlying competent rocks radially spreading above the flattening plastic unit. Consequently, polygonal faults are commonly characterized by a polygonal arrangement in map view. In our case, this geometry is not evident on a macro-scale map but is observable in the morpholineaments detailed map of the north-eastern Val d'Agri Basin (Di Niro and Giano, 1995), which displays a clear rhomboidal (i.e., polygonal) pattern along EAFS (Fig. 11).

Therefore, we propose that EAFS is partly polygonal. Specifically, regional macro-scale faults are mostly controlled by the regional NE-SW extensional tectonics and are well clustered. Conversely, meso-scale faults with limited extent at depth exhibit polygonal distribution (Fig. 12). If this novel interpretation is correct, the polygonal-like faults of Val d'Agri are among the few polygonal faults so far known in exposure. Commonly, polygonal faulting is identified in offshore basins with seismic data (e.g., Tewksbury et al., 2014; Petracchini et al., 2015). Furthermore, this model could likely be expanded to the Irpinia area (Fig. 1). Here, Ascione et al. (2013) proposed that short and discontinuously exposed faults with different attitude, kinematics, and maturity are confined at shallow structural levels, similarly to our meso-scale EAFS faults.

Along MMFS, both the macro-scale and meso-scale faults follow the

main regional tectonic trends (NW-SE and NE-SW; Fig. 3). Moreover, macro-scale faults are characterized by higher D values than those along EAFS (Fig. 5). Hence, we propose that faulting along the MMFS was mostly controlled by the regional extensional tectonics rather than polygonal faulting (Fig. 12), which, however, may explain a limited portion of the not-systematic attitude of fault surfaces and radial slip (Figs. 3 and 4b). The 3D thickness distribution of the Irpinia mélange is heterogeneous and partly unknown. Some previous studies suggest that the mélange tends to thin below the MMFS (Catalano et al., 2004; Mazzoli et al., 2014; Antoncecchi, 2020; Rinaldi et al., 2020). This inference may explain the different occurrence of polygonal-like faults beneath EAFS and MMFS as described above. This is also consistent with the fact that productive oil wells in the Val d'Agri are located on the eastern side of the basin. This suggests that the reservoir seal, provided by the Irpinia mélange unit, there is thick and mostly intact. Regarding this heterogeneous distribution of the Irpinia mélange, we speculate that macro-scale faults should easily cut downward across the mélange where it is thinner (mainly below the MMFS; Fig. 12). Instead, soft-linkage between shallow and deep structures is proposed to occur where the mélange is thicker (mainly below the EAFS; Fig. 12).

5.2. Relative timing of fault sets activity and tectonic evolution

The NE-SW- and NW-SE-striking faults represent the main regional tectonic trends of the Val d'Agri basin. Coherently with previous observations (Maschio et al., 2005; Bucci et al., 2012), the crosscutting relations documented for MMFS and EAFS show that the extensional NW-SE faults displace the extensional NE-SW faults (sites 2, 4, and 5 of Fig. 11), as well as most of the other differently striking faults (Fig. 2a and site 1 of Fig. 11). In addition, we report that high-angle normal to
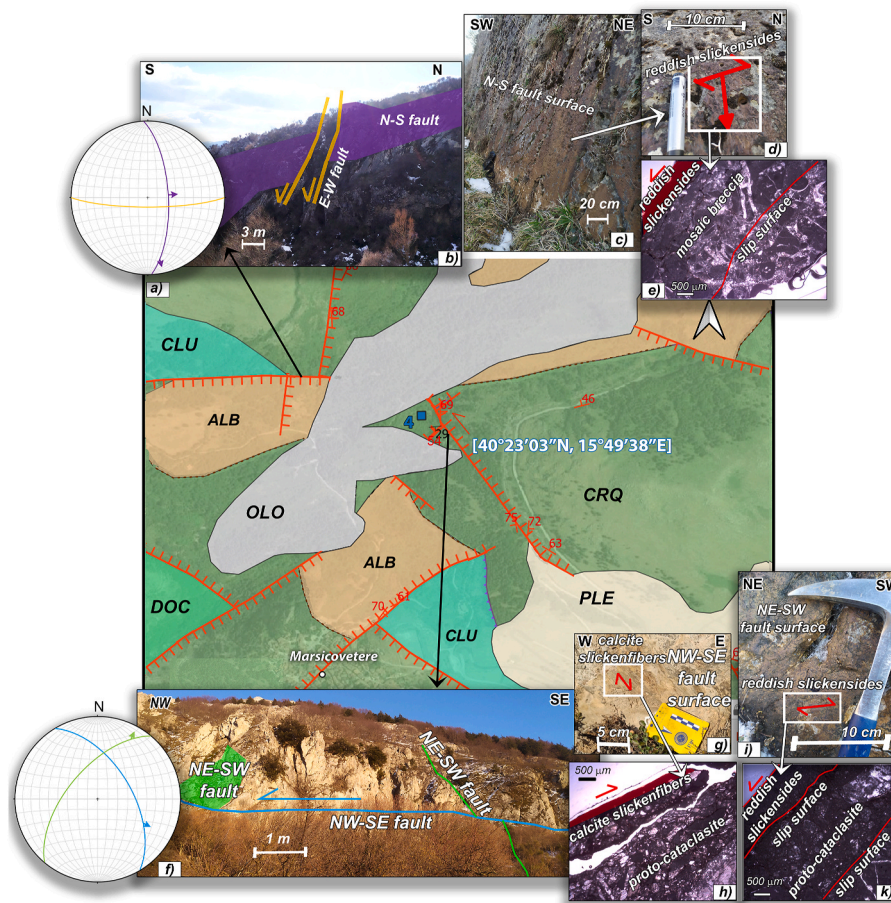
Fig. 9. a) Close-up view from Fig. 2 showing structural site 4 (40°23′03″N, 15°49′38″E). The outcropping formations are: Late Triassic-Paleocene undifferentiated dolomites (DOC), Late Triassic-Late Cretaceous Dolomitic limestones (CLU), Tithonian-Cenomanian Requienia and gastropods limestones (CRQ), Eocene-Early Miocene Albidona Fm. (ALB), Early-Middle Pleistocene alluvial deposits (PLE), and Late Pleistocene-Present Alluvial/slope detrital/lacustrine deposits (OLO). b) Outcrop and Schmidt projections (lower hemisphere) showing an E-W-striking normal fault (yellow) that displaces a N–S-striking normal to right-lateral fault (purple). c and d) Details of the N–S-striking fault surface coated with reddish slickensides. e) Optical microscopy image (parallel Nichols) of the reddish slickenfibers. f) Outcrop and Schmidt projections showing a NW-SE-striking left-lateral to right-oblique transtensional fault (blue) that displaces a NE-SW-striking right-lateral fault (green). g) Detail of the NW-SE-striking fault surface coated with calcite slickenfibers. h) Optical microscopy image (parallel Nichols) of the calcite slickenfibers. i) Detail of the NE-SW-striking fault surface coated with reddish slickensides. k) Optical microscopy image (parallel Nichols) of the reddish slickenfibers. Within all panels, red lines represent slip surfaces, and red arrows indicate slip directions and sense of motion. (For interpretation of the references to color in this figure legend, the reader is referred to the Web version of this article.)

right-lateral E-W striking faults crosscut both the N–S and NNE-SSW striking faults characterized by normal to lateral slip (Fig. 11, sites 1, 3, and 4). Furthermore, we show that the low-angle E-W striking normal faults, previously interpreted as syn-contractional gravitational collapses (Bucci et al., 2012, 2014), are displaced by the NE-SW striking normal faults (Fig. 7 and site 5 of Fig. 11). Finally, along the basin sides, the N–S striking low-angle thrusts are consistently displaced by the NE-SW, NW-SE, and E-W striking normal faults (Fig. 2a) and, in places, partly reactivated by NNE-SSW striking faults (Fig. 2a and 7, and site 2 of Fig. 11).

All pieces of evidence above indicate that the development of the Val d'Agri Basin was caused by extensional faulting along NW-SE striking faults and, subordinately, NE-SW striking faults. Both fault sets crosscut and partly reactivated the Late Miocene-Early Pleistocene orogenic structures, consisting of thrust faults, strike-slip faults, and low-angle extensional faults (Hippolyte et al., 1994; Monaco et al., 1998; Bucci et al., 2012, 2014; D'Adda et al., 2017; Manniello et al., 2023). The coeval activity of NE-SW and NW-SE extensional faults is fully consistent with present-day NE-SW crustal stretching (Mariucci and Montone, 2020), as observed in other extensional basins worldwide (e.g., Destro, 1995; Acocella and Funiciello, 2006). These regional extensional

tectonics are superimposed on or accompanied by local polygonal faulting, mainly observed in the EAFS (Fig. 12).

The new U–Pb ages of syn-tectonic calcite provide additional constraints on the tectonic evolution of the study area. In the Monte Aquila locality, the activity of the NW-SE-striking fault segment, exposed in the footwall of the main NW-SE-striking Mt. Aquila Fault, is Early-Middle Miocene (13.5 ± 2.47 Ma; Fig. 11). This age is considerably older than those assessed for the three post-orogenic slip events recognized along this fault, which were dated to Late Pleistocene-Holocene times through C^{14} dating of displaced paleosols (Improta et al., 2010). Coherently with structural observations in other fold and thrust belts worldwide (e.g., Bradley and Kidd, 1991; Ranero et al., 2003) as well as in central Apennines (Vitale et al., 2012; Mercuri et al., 2022) and with similar radiometrically dated pre-thrusting Middle Miocene extensional faults of the southern Apennines (Tavani et al., 2023), we ascribe this faulting phase to the forebulge-related stretching of the foreland lithosphere associated with the Adriatic plate subduction.

In contrast, near the Grumento Nova village, the activity of a NE-SW-striking right-lateral transtensional fault exposed in the hanging wall of a main ENE-WSW-striking normal fault is Middle Pleistocene-Holocene (0.82 ± 1.28 Ma; Fig. 11). This radiometric age is consistent with the
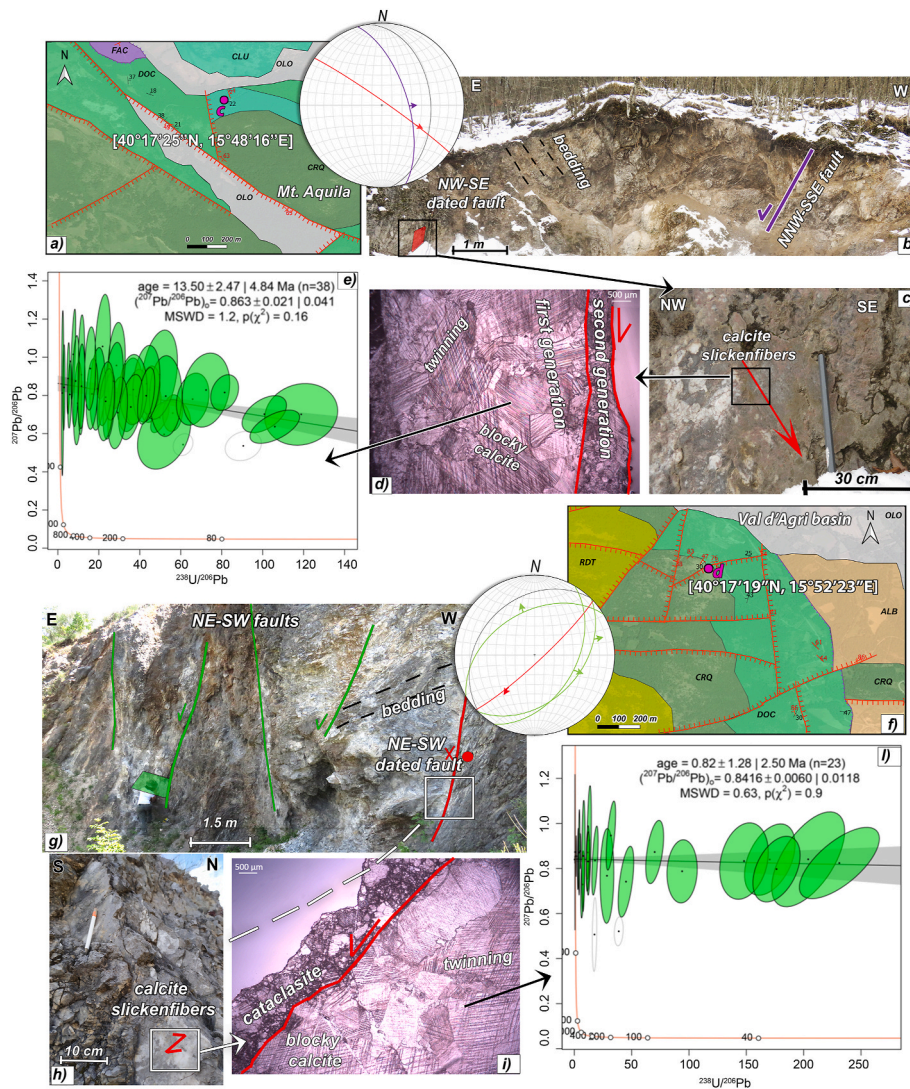
Fig. 10. a) Close-up view of Fig. 2 showing the location of the dated NW-SE-striking fault. b) Outcrop and Schmidt projections (lower hemisphere) of the dated fault (red). The photograph also shows the bedding attitude (black) and another NNW-SSE-striking normal fault (violet). c) Detail of the dated fault surface coated with calcite slickenfibers. d) Optical microscopy image (parallel Nichols) of the calcite slickenfibers. e) U–Pb Tera-Wasserburg plots for the older generation of calcite slickenfibres of Fig. 10d f) Close-up view from Fig. 2 showing the location of the dated NE-SW striking fault. g) Outcrop and Schmidt projections of the NE-SW-striking normal to transtensional fault segments. The photograph also shows the dated fault segment (red), other NE-SW-striking faults (green), and attitude of bedding (black). h) Detail of the dated fault surface coated with calcite slickenfibers. i) Optical microscopy image (parallel Nichols) of the calcite slickenfibers. l) U–Pb Tera-Wasserburg plots of the calcite slickenfibres in Fig. 10i. Within all panels, red lines represent slip surfaces, and red arrows indicate slip directions and sense of motion. FAC: Early Triassic Monte Facito Fm.; DOC: Late Triassic-Paleocene undifferentiated dolomites; CLU: Late Triassic-Late Cretaceous Dolomitic limestones; CRQ: Tithonian-Cenomanian Requienia and gastropods limestones; RDT: Cenomanian-Santonian Radiolitidae limestones; ALB: Eocene-Early Miocene Albidona Fm.; OLO: Late Pleistocene-Present Alluvial/slope detrital/lacustrine deposits. In U–Pb Tera-Wasserburg plots, the black line is the regression line that intercepts the concordia curve (orange line) with its 95% confidence intervals (grey bands). MSWD is the mean squared weighted deviation. (For interpretation of the references to color in this figure legend, the reader is referred to the Web version of this article.)

Middle Pleistocene-Holocene age proposed for post-orogenic extensional faulting based on geomorphological studies (Maschio et al., 2005; Zembo et al., 2009, 2011).

5.3. Seismotectonic implications

To compare the results of our structural analysis with the attitude of seismic sources in the study region, we consider the focal mechanisms of the 1971–2023 Mw ≥ 4.5 earthquakes (Gasparini et al., 1985; Cucci et al., 2004; Pondrelli et al., 2020; http://terremoti.ingv.it/) in the southern Apennines (Table S1; Fig. 13a), and of the 2001–2014 $1 \leq M_L \leq 2.9$ earthquakes in the Val d'Agri Basin (Improta et al., 2017, Fig. 13b–e). Data by Improta et al. (2017) are subdivided into natural clusters (Marsicovetere and Monti della Maddalena, Fig. 13b and d,

respectively) and manmade-induced clusters (Costa Molina 2 and Pertusillo Lake, Fig. 13c and e, respectively). We plot the attitude of nodal planes in rose diagrams (bin size 10°) as follows: 1) just one nodal plane (red) for focal mechanisms where the slip plane was already interpreted (Improta et al., 2017); 2) both nodal planes (grey) for other cases (Fig. 13).

The focal mechanisms of the strongest earthquakes in the southern Apennine (Fig. 13a) mostly display NW-SE striking normal faults with NE-SW oriented dip-slip motion, coherent with the present-day NE-SW tensional stress field (e.g., Maggi et al., 2009; Ferranti et al., 2009; Mariucci and Montone, 2020). In the Val d'Agri Basin, background seismicity is primarily enucleated within the Apulian Carbonate Platform in correspondence with high V_P/V_S ratio domains (Improta et al., 2017), and hence likely in association with high pore fluid pressure as
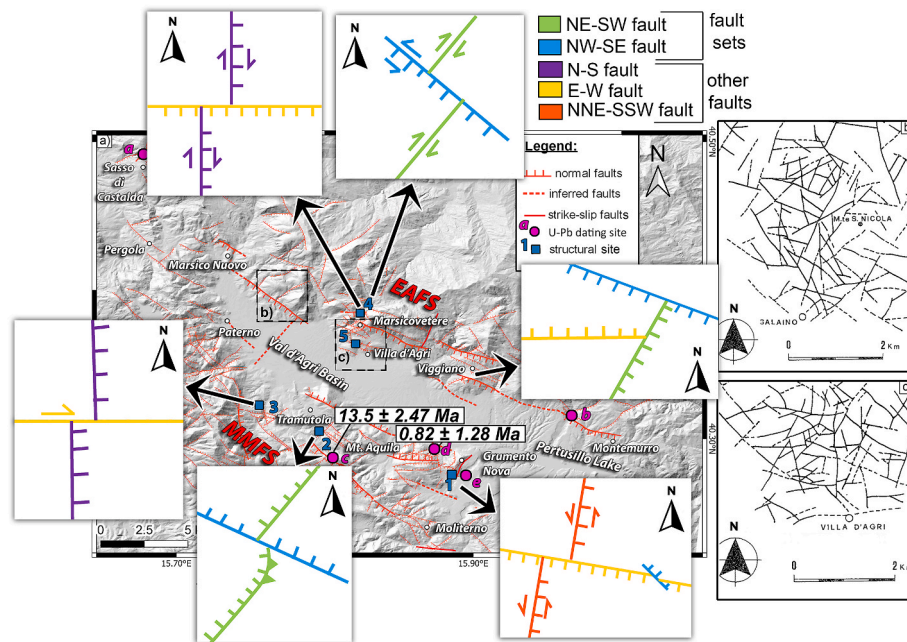
Fig. 11. a) Synthesis of the relative and absolute time relationship between faults. The five sketches show the fault cross-cutting relations described in Section 4.3, whereas the two ages are referred to as U–Pb dating described in Section 4.4. b) and c) Morpholineaments maps by Di Niro and Giano (1995).
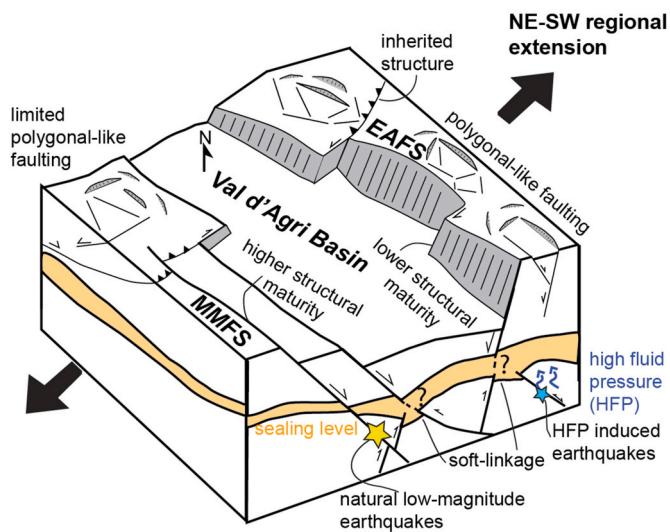

Fig. 12. Cartoon of the present-day Val d'Agri Basin fault architecture that shows: the macro-scale architecture and maturity; the meso-scale polygonal faulting (mainly developed in the EAFS); the natural low-magnitude background seismicity (mainly concentrated along the MMFS); and the high fluid pressure (HFP)-induced seismicity.

previously suggested for the Irpinia area (Amoroso et al., 2014). Natural microseismicity mainly pertains to the MMFS (Monti della Maddalena cluster; Fig. 13d). The results of the fault fractal analysis reported in this work show that the MMFS is characterized by higher structural maturity than the EAFS (Fig. 5). This is consistent with the 13-Ma-long tectonic activity constrained by U–Pb dating (Fig. 11). Cello et al. (2000) empirically correlated the higher structural maturity of the fault systems with the increasing magnitude of recorded earthquakes. In this regard, we note that the maturity degree computed for the MMFS (D = 1.19) is coherent with those (1.1 < D < 1.3) characterizing other active extensional fault systems of the Central Apennines (e.g., Norcia, Colfiorito, Mt. Gorzano, Mt. Vettore; Cello, 2000), able to enucleate strong and destructive earthquakes (5 ≤ Mw ≤ 6.7).

The Monti della Maddalena cluster is subdivided into deep events, located at depths of 10–12 km, and shallow events occurring at depths of 1–4 km (Fig. 13d). Nodal planes of the deep sub-cluster are interpreted as related to transtensional reactivation of a pre-existing NNE-SSW striking fault within the Paleozoic crystalline basement (Shiner et al., 2004; Mazzoli et al., 2013; D'Adda et al., 2017; Improta et al., 2017). Instead, the nodal planes of the shallow sub-cluster display a prevailing NW-SE strike distribution. They are interpreted as extensional activations of NW-SE-striking MMFS fault segments, likely correlated with Late Pleistocene-Holocene coseismic activity of the Mt. Aquila area (Fig. 13; Improta et al., 2010, 2017). Secondarily, natural seismicity occurred also along the EAFS (Marsicovetere clusters; Fig. 13b) at c. a. 6 km depth within the Apulian Carbonate Platform. Nodal planes from these focal mechanisms are interpreted as right-lateral reactivations of an inherited NE-SW striking transpressional blind fault (Improta et al., 2017). This fault, previously recognized by Nicolai and Gambini (2007), D'Adda et al. (2017), and Hager et al. (2021) through seismic interpretations, hosts pronounced methane near surface soil gas anomalies (Beaubien et al., 2023). In summary, fault plane solutions from natural low-magnitude events show that seismicity is mainly located along NW-SE-striking normal faults and secondarily along NE-SW-striking oblique faults (Fig. 13). Since these trends coincide with the main two sets of macro-scale EAFS and MMFS faults (Fig. 3), we highlight that, at the macro-scale, the fault system architecture generally reflects the geometry and kinematics of recent seismic sources. Furthermore, the coeval seismic activity of NW-SE and NE-SW striking faults suggests that they are active under the same NE-SW tensional stress field (Mariucci and Montone, 2020, Fig. 12).

Regarding the induced seismicity connected with artificially raised pore fluid pressure, nodal planes from these focal mechanisms do not show a systematic geometry, similarly with the outcomes of the EAFS meso-scale dataset. In detail, the seismic events pertaining to the induced Costa Molina 2 cluster, located along the EAFS at depths of 3–5 km (Fig. 13c), are interpreted as extensional to oblique reactivations (i.e., inversions) of a Pliocene NW-SE-striking back-thrust and of other small faults striking mostly E-W to NNW-SSE (Buttinelli et al., 2016; Improta et al., 2017). Instead, the Pertusillo Lake cluster, which
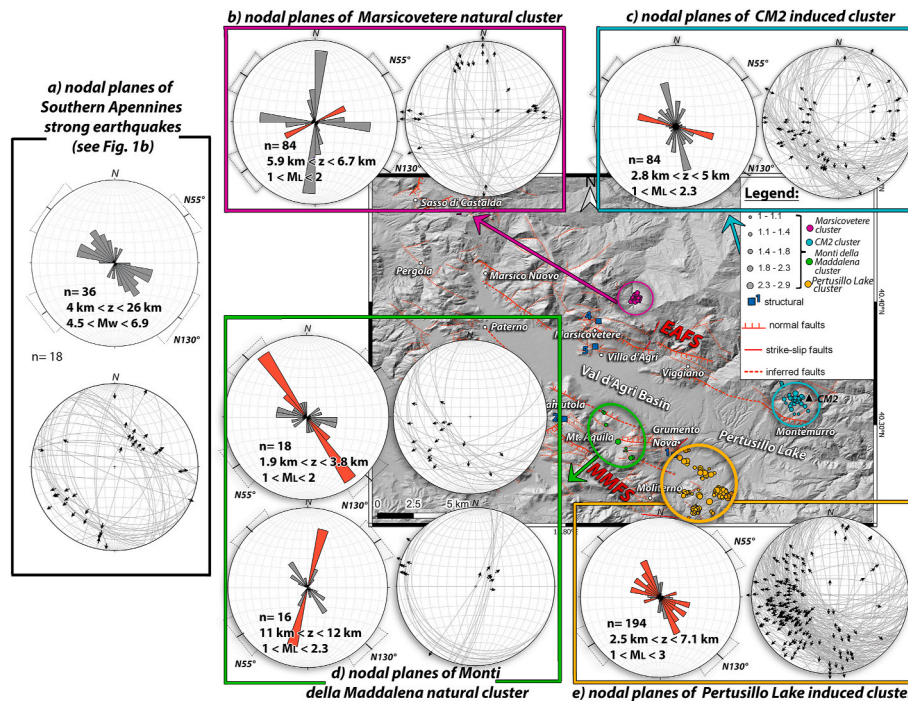
Fig. 13. Structural map of the Val d'Agri Basin with epicenters of low-magnitude earthquakes reported by Improta et al. (2017). Through different plots, we show: a) the attitude of nodal planes and related slip from recent strong regional earthquakes (southern Apennines); b) the attitude of nodal planes and related slip from the natural, low-magnitude Marsicovetere cluster of earthquakes. Note that the red peak in this and other rose diagrams represents the interpretation of seismic sources by Improta et al. (2017); c) attitude of nodal planes and related slip from induced, low-magnitude Costa Molina 2 (CM2) cluster of earthquakes; d) attitude of nodal planes and related slip from natural, low-magnitude Monti della Maddalena cluster of earthquakes; e) attitude of nodal planes and related slip from induced, low-magnitude Pertusillo Lake cluster of earthquakes. Within all rose diagrams, the bin size is 10°. (For interpretation of the references to color in this figure legend, the reader is referred to the Web version of this article.)

occurred at depths of 2–7 km along the MMFS (Fig. 13e), is interpreted as the extensional-to-oblique and right-lateral (re)activations of blind fault segments, respectively, striking NW-SE and NE-SW.

The high pore fluid pressure changes along the EAFS, induced by fluid injection within the Costa Molina 2 well (Improta et al., 2017; Hager et al., 2021; Roselli et al., 2023), as well as the high pore fluid pressure diffusion from the Pertusillo lake to the MMFS, induced by water level oscillations in combination with regional tectonics (Buttinelli et al., 2016; Improta et al., 2017; Picozzi et al., 2022), might have allowed the reactivation of less favorably oriented faults (e.g., Keranen et al., 2013; Scuderi and Collettini, 2016; Grigoli et al., 2018), previously generated by polygonal faulting or inherited by the complex tectonic evolution of the area (Fig. 12). Moreover, the distribution of manmade seismicity along the EAFS and MMFS was previously interpreted as the consequence of different rheological properties. Indeed, the mélange thickness >1 km that compartmentalized the reservoir beneath the EAFS did not permit the propagation of pore fluid perturbations from the Costa Molina 2 well toward the SW (Valoroso et al., 2023) and from the Pertusillo Lake toward the NE (Rinaldi et al., 2020).

6. Conclusions

The Val d'Agri Basin area hosts the largest onshore hydrocarbon field in Western Europe and constitutes a scientifically interesting and challenging natural laboratory for integrated structural and seismotectonic analyses. In fact, many geological, structural, and seismological studies were recently published on this area. Yet we believe there is still much room to better understand the past, present, and future relations among the inherited architecture of the fold-and-thrust belts, extensional faulting, and earthquake processes. The main results and new observations arising from the present study are the following.

1. The plastic Irpinia tectonic mélange lying beneath the allochthonous units and the Quaternary Val d'Agri Basin is interpreted as one of the main controlling factors of the structural architecture of the study area. In addition to the main NW-SE and NE-SW fault trends related to the ongoing post-orogenic extension, we recognized meso-scale polygonal-like style of faulting likely connected with the lateral spreading of rocks above the tectonic mélange. Indeed, we documented that this fault pattern is more developed along the northeastern side of the basin, where the mélange tends to be thicker. The seal capability of the Irpinia mélange provides efficient control on sub mélange pore fluid pressure and on its propagation, with implications for the triggering of natural and induced seismicity in the Val d'Agri Basin area.

2. We provided the first U–Pb ages of high-angle extensional fault zones in the Val d'Agri Basin area. The Holocene to Present activity of the MMFS involves faults active during Early-Middle Miocene that originated during the foreland flexure-related extensional faulting of the southern Apennine. These data, together with the crosscutting relations documented among the exposed large faults, confirm that the pre- and syn-compressional tectonic structures strongly influence present-day fault architecture of the Val d'Agri Basin.

3. Most natural low-magnitude earthquakes enucleate along the NW-SE striking fault system in the south-western side of the basin (MMFS) in response to the present NE-SW crustal stretching. This system is also characterized by a D value of 1.19, indicating high structural maturity (i.e., slip longevity). This spatial relationship between present seismicity and structural maturity is particularly interesting but not yet fully understood in view of seismic hazard evaluation, both in the Val d'Agri Basin area and elsewhere.

4. Manmade fluid pressure changes in the subsurface induce low-magnitude earthquakes that likely activate the numerous pre-existing and variably-oriented faults and take advantage of tectonic

stress connected with the ongoing extensional tectonics. Therefore, we delineate a complex seismotectonic framework for the Val d'Agri Basin, characterized by the interaction among local stress, inherited structures, polygonal faulting, and stress change induced by artificially-raised high fluid pressure.

5 Our structural study of the Val d'Agri demonstrates how the pattern of faults and therefore their seismic activation (both natural and induced) can be strongly controlled by the pre-existing tectono-stratigraphic architecture (i.e., tectonic history) and the rheology of the lithological components. These latter can indeed strongly influence the circulation of fluids (natural or artificially introduced), their pressures, and also the propagation of faults and their modes of activation.

CRediT authorship contribution statement

G. Schirripa Spagnolo: Conceptualization, Data curation, Formal analysis, Investigation, Methodology, Visualization, Writing – original draft. **F. Agosta:** Conceptualization, Formal analysis, Investigation, Writing – review & editing. **L. Aldega:** Conceptualization, Investigation, Writing – review & editing. **G. Prosser:** Conceptualization, Investigation, Writing – review & editing. **L. Smeraglia:** Conceptualization, Investigation, Writing – review & editing. **S. Tavani:** Conceptualization, Writing – review & editing. **N. Looser:** Investigation, Methodology, Writing – review & editing. **M. Guillong:** Methodology, Resources, Writing – review & editing. **S.M. Bernasconi:** Supervision, Writing – review & editing. **A. Billi:** Conceptualization, Methodology, Supervision, Writing – review & editing. **E. Carminati:** Conceptualization, Funding acquisition, Investigation, Methodology, Project administration, Supervision, Writing – review & editing.

Declaration of generative AI and AI-assisted technologies in the writing process

During the preparation of this work the author(s) used QUILLBOT in order to check grammatical errors. After using this tool/service, the author(s) reviewed and edited the content as needed and take(s) full responsibility for the content of the publication.

Declaration of competing interest

The authors declare that they have no known competing financial interests or personal relationships that could have appeared to influence the work reported in this paper.

Data availability

Table S2 of Supplementary Material.

Appendix A. Supplementary data

Supplementary data to this article can be found online at https://doi.org/10.1016/j.jsg.2024.105084.

References

Abdallah, I., Manniello, C., Prosser, G., Agosta, F., 2023. Regional scale structural architecture of basin-bounding faults in Mesozoic platform carbonates, southern Italy. J. Struct. Geol. 176, 104978 https://doi.org/10.1016/j.jsg.2023.104978.

Acocella, V., Funiciello, R., 2006. Transverse systems along the extensional Tyrrhenian margin of central Italy and their influence on volcanism. Tectonics 25 (2). https://doi.org/10.1029/2005TC001845.

Amoroso, O., Ascione, A., Mazzoli, S., Virieux, J., Zollo, A., 2014. Seismic imaging of a fluid storage in the actively extending Apennine mountain belt, southern Italy. Geophys. Res. Lett. 41 (11), 3802–3809. https://doi.org/10.1002/2014GL060070.

Antoncecchi, I., 2020. Modellazione geologico-strutturale 3D e sismicità indotta: il caso Val d'Agri. PhD Thesis., Dipartimento di Scienze della Terra. Università di Roma "La Sapienza", Rome. Retrieved from: https://iris.uniroma1.it/handle/11573/1623725.

Ascione, A., Mazzoli, S., Petrosino, P., Valente, E., 2013. A decoupled kinematic model for active normal faults: Insights from the 1980, MS= 6.9 Irpinia earthquake, southern Italy. Bulletin 125 (7–8), 1239–1259. https://doi.org/10.1130/B30814.1.

Bello, S., Lavecchia, G., Andrenacci, C., Ercoli, M., Cirillo, D., Carboni, F., Barchi, M.R., Brozzetti, F., 2022. Complex trans-ridge normal faults controlling large earthquakes. Sci. Rep. 12 (1), 1–20. https://doi.org/10.1038/s41598-022-14406-4.

Beaubien, S.E., Schirripa Spagnolo, G., Ridolfi, R.-M., Aldega, L., Antoncecchi, I., Bigi, S., Billi, A., Carminati, E., 2023. Structural control of gas migration pathways in the hydrocarbon-rich Val d'Agri basin (Southern Apennines, Italy). Mar. Petrol. Geol. 154, 106339 https://doi.org/10.1016/j.marpetgeo.2023.106339.

Benedetti, L., Tapponnier, P., King, G.C.P., Piccardi, L., 1998. Surface rupture of the 1857 southern Italian earthquake? Terra. Nova 10 (4), 206–210. https://doi.org/10.1046/j.1365-3121.1998.00189.x.

Bradley, D.C., Kidd, W.S.F., 1991. Flexural extension of the upper continental crust in collisional foredeeps. Geol. Soc. Am. Bull. 103, 1416–1438. https://doi.org/10.1130/0016-7606(1991)103<1416:FEOTUC>2.3.CO;2.

Brozzetti, F., 2011. The Campania-Lucania Extensional Fault System, southern Italy: a suggestion for a uniform model of active extension in the Italian Apennines. Tectonics 30 (5). https://doi.org/10.1029/2010TC002794.

Bonnet, E., Bour, O., Odling, N.E., Davy, P., Main, I., Cowie, P., Berkowitz, B., 2001. Scaling of fracture systems in geological media. Rev. Geophys. 39 (3), 347–383. https://doi.org/10.1029/1999RG000074.

Borraccini, F., De Donatis, M., Di Bucci, D., Mazzoli, S., 2002. 3D model of the active extensional fault system of the high Agri River valley, Southern Apennines, Italy. J. Virtual Explor. 6, 1–6.

Bucci, F., Novellino, R., Guglielmi, P., Prosser, G., Tavarnelli, E., 2012. Geological map of the northeastern sector of the high agri valley, southern Apennines (Basilicata, Italy). J. Maps 8 (3), 282–292. https://doi.org/10.1080/17445647.2012.722403.

Bucci, F., Novellino, R., Tavarnelli, E., Prosser, G., Guzzetti, F., Cardinali, M., Gueguen, E., Guglielmi, P., Adurno, I., 2014. Frontal collapse during thrust propagation in mountain belts: a case study in the Lucania Apennines, Southern Italy. J. Geol. Soc. 171 (4), 571–581. https://doi.org/10.1144/jgs2013-103.

Butler, R.W.H., Mazzoli, S., Corrado, S., De Donatis, M., Di Bucci, D., Gambini, R., Naso, G., Nicolai, C., Scrocca, D., Shiner, P., Zucconi, V., 2004. Applying Thick-Skinned Tectonic Models to the Apennine Thrust Belt of Italy—Limitations and Implications. https://doi.org/10.1306/M82813C34.

Buttinelli, M., Improta, L., Bagh, S., Chiarabba, C., 2016. Inversion of inherited thrusts by wastewater injection induced seismicity at the Val d'Agri oilfield (Italy). Sci. Rep. 6 (!), 37165. https://doi.org/10.1038/srep37165.

Caine, J.S., Evans, J.P., Forster, C.B., 1996. Fault zone architecture and permeability structure. Geology 24 (11), 1025–1028. https://doi.org/10.1130/0091-7613(1996)024<1025:FZAAPS>2.3.CO;2.

Candela, S., Mazzoli, S., Megna, A., Santini, S., 2015. Finite element modelling of stress field perturbations and interseismic crustal deformation in the Val d'Agri region, southern Apennines, Italy. Tectonophysics 657, 245–259. https://doi.org/10.1016/j.tecto.2015.07.011.

Carbone, S., Catalano, S., Lazzari, S., Lentini, F., Monaco, C., 1991. Presentazione della carta geologica del Bacino del Fiume Agri (Basilicata). Memor. Soc. Geol. Ital. 47, 129–143.

Carminati, E., Doglioni, C., 2012. Alps vs. Apennines: the paradigm of a tectonically asymmetric Earth. Earth Sci. Rev. 112 (1– 2), 67–96. https://doi.org/10.1016/j.earscirev.2012.02.004.

Cartwright, J., 2011. Diagenetically induced shear failure of fine-grained sediments and the development of polygonal fault systems. Mar. Petrol. Geol. 28 (9), 1593–1610. https://doi.org/10.1016/j.marpetgeo.2011.06.004.

Catalano, S., Monaco, C., Tortorici, L., Paltrinieri, W., Steel, N., 2004. Neogene-Quaternary tectonic evolution of the southern Apennines. Tectonics 23 (2). https://doi.org/10.1029/2003TC001512.

Ceccato, A., Tartaglia, G., Antonellini, M., Viola, G., 2022. Multiscale lineament analysis and permeability heterogeneity of fractured crystalline basement blocks. Solid Earth 13 (9), 1431–1453. https://doi.org/10.5194/se-13-1431-2022.

Cello, G., Mazzoli, S., 1998. Apennine tectonics in southern Italy: a review. J. Geodyn. 27 (2), 191–211. https://doi.org/10.1016/S0264-3707(97)00072-0.

Cello, G., 2000. A quantitative structural approach to the study of active fault zones in the Apennines (peninsular Italy). J. Geodyn. 29 (3–5), 265–292. https://doi.org/10.1016/S0264-3707(99)00044-7.

Cello, G., Gambini, R., Mazzoli, S., Read, A., Tondi, E., Zucconi, V., 2000. Fault zone characteristics and scaling properties of the val d'Agri Fault system (southern Apennines, Italy). J. Geodyn. 29 (3–5), 293–307. https://doi.org/10.1016/S0264-3707(99)00043-5.

Cello, G., Tondi, E., Micarelli, L., Mattioni, L., 2003. Active tectonics and earthquake sources in the epicentral area of the 1857 Basilicata earthquake (southern Italy). J. Geodyn. 36 (1–2), 37–50. https://doi.org/10.1016/S0264-3707(03)00037-1.

Cladouhos, T.T., Marrett, R., 1996. Are fault growth and linkage models consistent with power-law distributions of fault lengths? J. Struct. Geol. 18 (2–3), 281–293. https://doi.org/10.1016/S0191-8141(96)80050-2.

Corrado, S., Aldega, L., Di Leo, P., Giampaolo, C., Invernizzi, C., Mazzoli, S., Zattin, M., 2005. Thermal maturity of the axial zone of the Southern Apennines fold-and-thrust-belt (Italy) from multiple organic and inorganic indicators. Terra. Nova 17 (1), 56–65. https://doi.org/10.1111/j.1365-3121.2004.00584.x.

Barchi, M., Amato, A., Cippitelli, G., Merlini, S., Montone, P., 2007. Extensional tectonics and seismicity in the axial zone of the Southern Apennines. Boll. Soc. Geol. It. (Italian Journal of Geosciences) 47–56. Special Issues (7). Retrieved from: https://www.earth-prints.org/handle/2122/2980.

CPTI, 2022. Catalogo Parametrico dei Terremoti Italiani, INGV. Retrieved from: http://emidius.mi.ingv.it/CPTI15-DBMI15/.

Cucci, L., Pondrelli, S., Frepoli, A., Mariucci, M.T., Moro, M., 2004. Local pattern of stress field and seismogenic sources in the Pergola–Melandro basin and the Agri valley (Southern Italy). Geophys. J. Int. 156 (3), 575–583. https://doi.org/10.1111/j.1365-246X.2004.02161.x.

D'Adda, P., Longoni, R., Magistroni, C., Meda, M., Righetti, F., Cavozzi, C., Nestola, Y., Storti, F., 2017. Extensional reactivation of a deep transpressional architecture: Insights from sandbox analogue modeling applied to the Val d'Agri basin (Southern Apennines, Italy). Interpretation 5 (1), SD55–SD66. https://doi.org/10.1190/INT-2016-0078.1.

Destro, N., 1995. Release fault: a variety of cross fault in linked extensional fault systems, in the Sergipe-Alagoas Basin, NE Brazil. J. Struct. Geol. 17 (5), 615–629. https://doi.org/10.1016/0191-8141(94)00088-H.

Di Niro, A., & Giano, S. I. (1995). Evoluzione geomorfologica del bordo orientale dell'Alta Val d'Agri (Basilicata). *STUDI GEOLOGICI CAMERTI. NUOVA SERIE*, *1995*, 207-218.

Doglioni, C., Mongelli, F., Pieri, P., 1994. The Puglia uplift (SE Italy): an anomaly in the foreland of the Apenninic subduction due to buckling of a thick continental lithosphere. Tectonics 13 (5), 1309–1321. https://doi.org/10.1029/94TC01501.

Doglioni, C., 1995. Geological remarks on the relationships between extension and convergent geodynamic settings. Tectonophysics 252, 253–267. https://doi.org/10.1016/0040-1951(95)00087-9.

Elmahdy, M., Tarabees, E., Bakr, A., Farag, A.E., 2020. Polygonal faults in Eocene carbonate reservoir, Abu El-Gharadig basin, Egypt. Geol. J. 55 (6), 4670–4680. https://doi.org/10.1002/gj.3708.

Ferranti, L., Santoro, E., Mazzella, M.E., Monaco, C., Morelli, D., 2009. Active transpression in the northern Calabria Apennines, southern Italy. Tectonophysics 476 (1–2), 226–251. https://doi.org/10.1016/j.tecto.2008.11.010.

Gasparini, C., Iannaccone, G., Scarpa, R., 1985. Fault-plane solutions and seismicity of the Italian peninsula. Tectonophysics 117, 59–78. https://doi.org/10.1016/0040-1951(85)90236-7.

Giano, S.I., Maschio, L., Alessio, M., Ferranti, L., Improta, S., Schiattarella, M., 2000. Radiocarbon dating of active faulting in the Agri high valley, southern Italy. J. Geodyn. 29 (3–5), 371–386. https://doi.org/10.1016/S0264-3707(99)00058-7.

Grigoli, F., Cesca, S., Rinaldi, A.P., Manconi, A., Lopez-Comino, J.A., Clinton, J.F., Westaway, R., Cauzzi, C., Dahm, T., Wiemer, S., 2018. The November 2017 M w 5.5 Pohang earthquake: a possible case of induced seismicity in South Korea. Science 360 (6392), 1003–1006. https://doi.org/10.1126/science.aat2010.

Guillong, M., Wotzlaw, J., Looser, N., Laurent, O., 2020. Evaluating the reliability of U–Pb laser ablation inductively coupled plasma mass spectrometry (LA-ICP-MS) carbonate geochronology: matrix issues and a potential calcite validation reference material. Geochronology 2, 155–167. https://doi.org/10.5194/gchron-2-155-2020.

Hager, B.H., Dieterich, J., Frohlich, C., Juanes, R., Mantica, S., Shaw, J.H., Bottazzi, F., Caresani, F., Castineira, D., Cominelli, A., Mesa, M., Osculati, L., Petroselli, S., Plesch, A., 2021. A process-based approach to understanding and managing triggered seismicity. Nature 595 (7869), 684–689. https://doi.org/10.1038/s41586-021-03668-z.

Hippolyte, J.C., Angelier, J., Roure, F.B., 1994. A major geodynamic change revealed by Quaternary stress patterns in the Southern Apennines (Italy). Tectonophysics 230 (3–4), 199–210. https://doi.org/10.1016/0040-1951(94)90135-X.

Improta, L., Ferranti, L., De Martini, P.M., Piscitelli, S., Bruno, P.P., Burrato, P., Civico, R., Giocoli, A., Iorio, M., D'Addezio, G., Maschio, L., 2010. Detecting young, slow-slipping active faults by geologic and multidisciplinary high-resolution geophysical investigations: a case study from the Apennine seismic belt, Italy. J. Geophys. Res. Solid Earth 115 (B11). https://doi.org/10.1029/2010JB000871.

Improta, L., Bagh, S., De Gori, P., Valoroso, L., Pastori, M., Piccinini, D., Chiarabba, C., Anselmi, M., Buttinelli, M., 2017. Reservoir structure and wastewater-induced seismicity at the Val d'Agri Oilfield (Italy) shown by three-dimensional Vp and Vp/Vs local earthquake tomography. J. Geophys. Res. Solid Earth 122 (11), 9050–9082. https://doi.org/10.1002/2017JB014725.

Keranen, K.M., Savage, H.M., Abers, G.A., Cochran, E.S., 2013. Potentially induced earthquakes in Oklahoma, USA: links between wastewater injection and the 2011 Mw 5.7 earthquake sequence. Geology 41 (6), 699–702. https://doi.org/10.1130/G34045.1.

Leonard, M., 2010. Earthquake fault scaling: self-consistent relating of rupture length, width, average displacement, and moment release. Bull. Seismol. Soc. Am. 100 (5A), 1971–1988. https://doi.org/10.1785/0120090189.

Lentini, F., Carbone, S., Catalano, S., Monaco, C., 1987. Confronti sedimentologico-petrografici e posozione strutturale dei Flysch di Albidona e di Gorgaglione nella media Val d'Agri (Appennino Lucano). Memor. Soc. Geol. Ital. 38, 259–273.

Maggi, C., Frepoli, A., Cimini, G.B., Console, R., Chiappini, M., 2009. Recent seismicity and crustal stress field in the Lucanian Apennines and surrounding areas (Southern Italy): seismotectonic implications. Tectonophysics 463 (1–4), 130–144. https://doi.org/10.1016/j.tecto.2008.09.032.

Malinverno, A., Ryan, W.B., 1986. Extension in the Tyrrhenian Sea and shortening in the Apennines as result of arc migration driven by sinking of the lithosphere. Tectonics 5 (2), 227–245. https://doi.org/10.1029/TC005i002p00227.

Mallet, R., 1862. *Great Neapolitan earthquake of 1857: the first principles of observational seismology as developed in the report. In: to the Royal Society of London of the expedition made by command of the King of the Kingdom of Naples, to investigate the circumstances of the great earthquake of December 1857*, (Vol. 2).. Chapman and Hall.

Manighetti, I., Campillo, M., Bouley, S., Cotton, F., 2007. Earthquake scaling, fault segmentation, and structural maturity. Earth Planet Sci. Lett. 253 (3–4), 429–438. https://doi.org/10.1016/j.epsl.2006.11.004.

Manighetti, I., Mercier, A., De Barros, L., 2021. Fault trace corrugation and segmentation as a measure of fault structural maturity. Geophys. Res. Lett. 48 (20), e2021GL095372 https://doi.org/10.1029/2021GL095372.

Manniello, C., Abdallah, I., Prosser, G., Agosta, F., 2023. Pressure solution-assisted diagenesis and thrusting-related deformation of Mesozoic platform carbonates. J. Struct. Geol. 173, 104906 https://doi.org/10.1016/j.jsg.2023.104906.

Marchegiani, L., Van Dijk, J.P., Gillespie, P.A., Tondi, E., Cello, G., 2006. Scaling properties of the dimensional and spatial characteristics of fault and fracture systems in the Majella Mountain, central Italy. Geological Society, London, Special Publications 261 (1), 113–131. https://doi.org/10.1144/GSL.SP.2006.261.01.09.

Mariucci, M.T., Montone, P., 2020. Database of Italian present-day stress indicators, IPSI 1.4. Sci. Data 7 (1), 298. https://doi.org/10.1038/s41597-020-00640-w.

Maschio, L., Ferranti, L., Burrato, P., 2005. Active extension in Val d'Agri area, Southern Apennines, Italy: implications for the geometry of the seismogenic belt. Geophys. J. Int. 162 (2), 591–609. https://doi.org/10.1111/j.1365-246X.2005.02597.x.

Mazzoli, S., Barkham, S., Cello, G., Gambini, R., Mattioni, L., Shiner, P., Tondi, E., 2001. Reconstruction of continental margin architecture deformed by the contraction of the Lagonegro Basin, southern Apennines, Italy. J. Geol. Soc. 158 (2), 309–319. https://doi.org/10.1144/jgs.158.2.309.

Mazzoli, S., D'errico, M., Aldega, L., Corrado, S., Invernizzi, C., Shiner, P., Zattin, M., 2008. Tectonic burial and "young"(< 10 Ma) exhumation in the southern Apennines fold-and-thrust belt (Italy). Geology 36 (3), 243–246. https://doi.org/10.1130/G24344A.1.

Mazzoli, S., Ascione, A., Candela, S., Iannace, A., Megna, A., Santini, S., Vitale, S., 2013. Subduction and continental collision events in the southern Apennines: constraints from two crustal cross-sections. Rendiconti Online della Società Geologica Italiana 25, 78–84. Retrieved from: https://www.researchgate.net/publication/281647624.

Mazzoli, S., Ascione, A., Buscher, J.T., Pignalosa, A., Valente, E., Zattin, M., 2014. Low-angle normal faulting and focused exhumation associated with late Pliocene change in tectonic style in the southern Apennines (Italy). Tectonics 33 (9), 1802–1818. https://doi.org/10.1002/2014TC003608.

Mercuri, M., Smeraglia, L., Curzi, M., Tavani, S., Maffucci, R., Pignalosa, A., Billi, A., Carminati, E., 2022. Pre-folding fracturing in a foredeep environment: insights from the Carseolani Mountains (central Apennines, Italy). Geol. Mag. 159 (11–12), 1897–1913. https://doi.org/10.1017/S0016756821001291.

Monaco, C., Tortorici, L., Paltrinieri, W., 1998. Structural evolution of the Lucanian Apennines, southern Italy. J. Struct. Geol. 20 (5), 617–638. https://doi.org/10.1016/S0191-8141(97)00105-3.

Montone, P., Mariucci, M.T., Pondrelli, S., Amato, A., 2004. An improved stress map for Italy and surrounding regions (central Mediterranean). J. Geophys. Res. Solid Earth 109 (B10). https://doi.org/10.1029/2003JB002703.

Nicolai, C., Gambini, R., 2007. Structural architecture of the Adria platform-and-basin system. Boll. Soc. Geol. Ital. 7, 21–37. Retrieved from: https://www.researchgate.net/profile/Roberto-Gambini/publication/277015552_Structural_architecture_of_the_Adria_platform-and-basin_system/links/55631dfc08ae9963a11b7473/Structural-architecture-of-the-Adria-platform-and-basin-system.pdf.

Nyberg, B., Nixon, C.W., Sanderson, D.J., 2018. NetworkGT: a GIS tool for geometric and topological analyses of two-dimensional fracture networks. Geosphere 14, 1618–1634. https://doi.org/10.1130/ges01595.1.

Ortega, O.J., Marrett, R.A., Laubach, S.E., 2006. A scale-independent approach to fracture intensity and average spacing measurement. AAPG bulletin 90 (2), 193–208. https://doi.org/10.1306/08250505059.

Palladino, G., Prosser, G., Olita, F., Avagliano, D., Dello Iacovo, B., Giano, S.I., Bentivenga, M., Agosta, F., Grimaldi, S., 2023. Reconstruction of the structural setting of the north-eastern side of the high Agri Valley (Southern Apennines, Italy) based on detailed field mapping. J. Maps 19 (1), 2257729. https://doi.org/10.1080/17445647.2023.2257729.

Patacca, E., Scandone, P., 2007. Geology of the southern Apennines. Boll. Soc. Geol. Ital. 7, 75–119.

Peacock, D.C.P., Sanderson, D.J., 2018. Structural analyses and fracture network characterisation: seven pillars of wisdom. Earth Sci. Rev. 184, 13–28. https://doi.org/10.1016/j.earscirev.2018.06.006.

Petracchini, L., Antonellini, M., Billi, A., Scrocca, D., 2015. Syn-thrusting polygonal normal faults exposed in the hinge of the Cingoli anticline, northern Apennines, Italy. Front. Earth Sci. 3, 67. https://doi.org/10.3389/feart.2015.00067.

Picozzi, M., Serlenga, V., Stabile, T.A., 2022. Spatio-temporal evolution of ground motion intensity caused by reservoir-induced seismicity at the Pertusillo artificial lake (southern Italy). Front. Earth Sci. 10, 1048196 https://doi.org/10.3389/feart.2022.1048196.

Pondrelli, S., Visini, F., Rovida, A., D'Amico, V., Pace, B., Meletti, C., 2020. Style of faulting of expected earthquakes in Italy as an input for seismic hazard modeling. Nat. Hazards Earth Syst. Sci. 20 (12), 3577–3592. https://doi.org/10.5194/nhess-20-3577-2020.

Prosser, G., Palladino, G., Avagliano, D., Coraggio, F., Bolla, E.M., Riva, M., Catellani, D. E., 2021. Stratigraphic and tectonic setting of the Liguride units cropping out along the southeastern side of the Agri Valley (Southern Apennines, Italy). Geosciences 11 (3), 125. https://doi.org/10.3390/geosciences11030125.

Ranero, C.R., Morgan, J.P., McIntosh, K., Reichert, C., 2003. Bending-related faulting and mantle serpentinization at the Middle America trench. Nature 425, 367–373. https://doi.org/10.1038/nature01961.

Rinaldi, A.P., Improta, L., Hainzl, S., Catalli, F., Urpi, L., Wiemer, S., 2020. Combined approach of poroelastic and earthquake nucleation applied to the reservoir-induced seismic activity in the Val d'Agri area, Italy. J. Rock Mech. Geotech. Eng. 12 (4), 802–810. https://doi.org/10.1016/j.jrmge.2020.04.003.

Roberts, N.M.W., Rasbury, E.T., Parrish, R.R., Smith, C.J., Horstwood, M.S.A., Condon, D.J., 2017. A calcite reference material for LA-ICP-MS U-Pb geochronology. G-cubed 18, 2807–2814. https://doi.org/10.1002/2016GC006784.

Roselli, P., Improta, L., Kwiatek, G., Martínez-Garzón, P., Saccorotti, G., Lombardi, A.M., 2023. Source mechanisms and induced seismicity in the Val d'Agri Basin (Italy). Geophys. J. Int. 234 (3), 1617–1627. https://doi.org/10.1093/gji/ggad155.

Roure, F., Casero, P., Vially, R., 1991. Growth processes and melange formation in the southern Apennines accretionary wedge. Earth Planet Sci. Lett. 102 (3–4), 395–412. https://doi.org/10.1016/0012-821X(91)90031-C.

Scrocca, D., Carminati, E., Doglioni, C., 2005. Deep structure of the southern Apennines, Italy: thin-skinned or thick-skinned? Tectonics 24 (3). https://doi.org/10.1029/2004TC001634.

Scuderi, M.M., Collettini, C., 2016. The role of fluid pressure in induced vs. triggered seismicity: insights from rock deformation experiments on carbonates. Sci. Rep. 6 (1), 1–9. https://doi.org/10.1038/srep24852.

Sibson, R.H., 2020. Preparation zones for large crustal earthquakes consequent on fault-valve action. Earth Planets Space 72, 1–20. https://doi.org/10.1186/s40623-020-01153-x.

Smeraglia, L., Mercuri, M., Tavani, S., Pignalosa, A., Kettermann, M., Billi, A., Carminati, E., 2021. 3D Discrete Fracture Network (DFN) models of damage zone fluid corridors within a reservoir-scale normal fault in carbonates: multiscale approach using field data and UAV imagery. Mar. Petrol. Geol. 126, 104902 https://doi.org/10.1016/j.marpetgeo.2021.104902.

Shiner, P., Beccacini, A., Mazzoli, S., 2004. Thin-skinned versus thick-skinned structural models for Apulian carbonate reservoirs: constraints from the Val d'Agri Fields, S Apennines, Italy. Mar. Petrol. Geol. 21 (7), 805–827. https://doi.org/10.1016/j.marpetgeo.2003.11.020.

Spyropoulos, C., Griffith, W.J., Scholz, C.H., Shaw, B.E., 1999. Experimental evidence for different strain regimes of crack populations in a clay model. Geophys. Res. Lett. 26 (8), 1081–1084. https://doi.org/10.1029/1999GL900175.

Stabile, T.A., Giocoli, A., Lapenna, V., Perrone, A., Piscitelli, S., Telesca, L., 2014. Evidence of low-magnitude continued reservoir-induced seismicity associated with the Pertusillo Artificial Lake (southern Italy). Bull. Seismol. Soc. Am. 104 (4), 1820–1828. https://doi.org/10.1785/0120130333.

Stabile, T.A., Vlček, J., Wcisło, M., Serlenga, V., 2021. Analysis of the 2016–2018 fluid-injection induced seismicity in the High Agri Valley (Southern Italy) from improved detections using template matching. Sci. Rep. 11 (1), 20630 https://doi.org/10.1038/s41598-021-00047-6.

Tarquini S., Isola I., Favalli M., Battistini A., 2007. TINITALY, a digital elevation model of Italy with a 10 m-cell size (Version 1.0). Istituto Nazionale di Geofisica e Vulcanologia (INGV). https://doi.org/10.13127/TINITALY/1.0.

Tavani, S., Ogata, K., Vinci, F., Sabbatino, M., Kylander-Clark, A., Caterino, G., Buglione, A., Cibelli, A., Maresca, A., Iacopini, D., Parente, M., Iannace, A., 2023. Post-rift Aptian-Cenomanian extension in Adria, insight from the km-scale Positano-Vico Equense syn-sedimentary fault. J. Struct. Geol. 168, 104820 https://doi.org/10.1016/j.jsg.2023.104820.

Tewksbury, B.J., Hogan, J.P., Kattenhorn, S.A., Mehrtens, C.J., Tarabees, E.A., 2014. Polygonal faults in chalk: insights from extensive exposures of the Khoman formation, western Desert, Egypt. Geology 42 (6), 479–482. https://doi.org/10.1130/G35362.1.

Valoroso, L., Improta, L., Chiaraluce, L., Di Stefano, R., Ferranti, L., Govoni, A., Chiarabba, C., 2009. Active faults and induced seismicity in the Val d'Agri area (Southern Apennines, Italy). Geophys. J. Int. 178 (1), 488–502. https://doi.org/10.1111/j.1365-246X.2009.04166.

Valoroso, L., Piccinini, D., Improta, L., Gaviano, S., Giunchi, C., 2023. Characterizing seismogenic fault structures of the lake Pertusillo reservoir induced seismicity (southern Italy) using a relocated template-matching catalog. J. Geophys. Res. Solid Earth 128 (7), e2022JB025879. https://doi.org/10.1029/2022JB025879.

Vermeesch, P., 2018. IsoplotR: a free and open toolbox for geochronology. Geosci. Front. 9, 1479–1493. https://doi.org/10.1016/j.gsf.2018.04.001.

Vezzani, L., Festa, A., Ghisetti, F., 2010. Geological-structural map of the central-southern Apennines (Italy). scale 1, 250.

Vitale, S., Dati, F., Mazzoli, S., Ciarcia, S., Guerriero, V., Iannace, A., 2012. Modes and timing of fracture network development in poly-deformed carbonate reservoir analogues, Mt. Chianello, southern Italy. J. Struct. Geol. 37, 223–235. https://doi.org/10.1016/j.jsg.2012.01.005.

Vitale, S., Ciarcia, S., 2018. Tectono-stratigraphic setting of the Campania region (southern Italy). J. Maps 14 (2), 9–21. https://doi.org/10.1080/17445647.2018.1424655.

Wells, D.L., Coppersmith, K.J., 1994. New empirical relationships among magnitude, rupture length, rupture width, rupture area, and surface displacement. Bull. Seismol. Soc. Am. 84 (4), 974–1002. Retrieved from. https://pubs.geoscienceworld.org/ssa/bssa/article-abstract/84/4/974/119792/New-empirical-relationships-among-magnitude?redirectedFrom=fulltext.

Xia, Y., Yang, J., Chen, Y., Lu, S., Wang, M., Deng, S., Yao, Z., Lu, M., 2022. A review of the global polygonal faults: are they playing a big role in fluid migration? Front. Earth Sci. 9, 1323. https://doi.org/10.3389/feart.2021.786915.

Zembo, I., Panzeri, L., Galli, A., Bersezio, R., Martini, M., Sibilia, E., 2009. Quaternary evolution of the intermontane val D'Agri Basin, southern Apennines. Quat. Res. 72 (3), 431–442. https://doi.org/10.1016/j.yqres.2009.02.009.

Zembo, I., Vignola, P., Andò, S., Bersezio, R., Vezzoli, L., 2011. Tephrochronological study in the quaternary Val d'Agri intermontane basin (Southern Apennines, Italy). Int. J. Earth Sci. 100 (1), 173–187. https://doi.org/10.1007/s00531-009-0501-x.